Water Resources Research

RESEARCH ARTICLE
10.1029/2020WR027585

Efficiency and Accuracy of Micro-Macro Models for Mineral Dissolution

Stephan Gärttner[1], Peter Frolkovič[2], Peter Knabner[1], and Nadja Ray[1]

[1]Department of Mathematics, Friedrich-Alexander University Erlangen-Nürnberg, Erlangen, Germany, [2]Faculty of Civil Engineering, Slovak University of Technology, Bratislava, Slovakia

Key Points:
- We investigate reactive flow and transport problems for mineral dissolution
- A fully coupled nonlinear micro-macro model is considered including evolving microstructures by means of level-set methods
- Taking advantage of parallel computing and a tailored adaptivity scheme, computation times are comparable to purely macroscopic simulations

Correspondence to:
S. Gärttner,
gaerttner@math.fau.de

Citation:
Gärttner, S., Frolkovič, P., Knabner, P., & Ray, N. (2020). Efficiency and accuracy of micro-macro models for mineral dissolution. *Water Resources Research*, *56*, e2020WR027585. https://doi.org/10.1029/2020WR027585

Received 25 MAR 2020
Accepted 27 JUL 2020
Accepted article online 15 AUG 2020

Abstract Micro-macro models for dissolution processes are derived from detailed pore-scale models applying upscaling techniques. They consist of flow and transport equations at the scale of the porous medium (macroscale). Both include averaged time- and space-dependent coefficient functions (permeability, porosity, reactive surface, and effective diffusion). These are in turn explicitly computed from the time- and space-dependent geometry of unit cells and by means of auxiliary cell problems defined therein (microscale). The explicit geometric structure is characterized by a level set. For its evolution, information from the transport equations solutions is taken into account (micro-macro scales). A numerical scheme is introduced, which is capable of evaluating such complex settings. For the level-set equation a second-order scheme is applied, which enables us to accurately determine the dynamic reactive surface. Local mesh refinement methods are applied to evaluate Stokes type cell problems using P_2/P_1 elements and a Uzawa type linear solver. Applications of our permeability solver to scenarios involving static and evolving geometries are presented. Furthermore, macroscopic flow and transport equations are solved applying mixed finite elements. Finally, adaptive strategies to overcome the computational burden are discussed. We apply our approach to the dissolution of an array of dolomite grains in the micro-macro context and validate our numerical scheme.

1. Introduction

Porous media applications naturally exhibit at least two different spatial scales, on which measurements, modeling, and simulations are possible: The pore scale/microscale is the fundamental scale, on which processes take place with pore (void) space and solid being distinguishable. On the other hand, the macroscale/continuum scale, that is, the scale of the porous medium, is ultimately of practical relevance for reactive transport computations. However, geochemical behavior cannot be understood considering this larger scale alone and investigations become increasingly difficult if the dynamically evolving pore-scale structure is taken into account. Approaching such situations, pore network models (Xiong et al., 2016), hybrid models (Battiato et al., 2011; Tartakovsky et al., 2008), microcontinuum models (Soulaine et al., 2017, 2018), and micro-macro models (Bringedal et al., 2019; Ray, Oberlander, et al., 2019; van Noorden, 2009a) are available in the literature. For recent reviews in the context of reactive transport modeling, we further refer to Steefel et al. (2015) and Molins and Knabner (2019).

In this research we focus on micro-macro models resulting from averaging theory, which are additionally capable of representing evolving interfaces. We numerically investigate a micro-macro model similar to that stated in Ray, Oberlander, et al. (2019) and van Noorden (2009a). In this model, mineral precipitation and dissolution reactions alter the porous medium's structure. More precisely, dissolved chemical species are transported by convection and diffusion through the porous medium and react to a mineral with nonnegligible volume fraction and density ρ. The micro-macro model then consists of flow and transport equations for the species' concentrations at the scale of the porous medium (macroscale). Both include averaged time- and space-dependent parameters such as permeability, porosity, reactive surface, and effective diffusion tensor. These parameters are deduced from unit cells with evolving geometries and auxiliary cell problems defined therein (microscale). Structural changes of the underlying geometry due to the dissolution reactions as well as the interface between the mineral and the liquid are characterized by means of a level set, which is a classical way to include evolving interfaces into a model. An extension of formal two-scale asymptotic expansion including a level-set description for an evolving solid-liquid interface was introduced in van Noorden (2009a, 2009b). This method has been applied to precipitation/dissolution reactions (van Noorden, 2009a, 2009b;

van Noorden et al., 2010), locally periodic media (Muntean & van Noorden, 2013), biofilm growth (Ebigbo et al., 2010; Schulz & Knabner, 2017a, 2017b), nonisothermal reactive flow (Bringedal et al., 2016), colloid dynamics (Ray et al., 2012), drug delivery (Ray et al., 2013), and reactive flows under dominant convection in (Kumar et al., 2011; Ray & Schulz, 2019). On the other hand, information from the macroscopic transport equations solutions is taken into account to determine the level-set evolution (micro-macro scale). If applicable an ansatz similar to the one proposed in Ray, Oberlander, et al. (2019) is applied to include the impact of the magnitude and direction of the flow velocity on the dissolution pattern. Since the overall model comprises several levels of couplings (cf. Figure 2a), thus far, mainly restrictive geometrical settings, for example, radially symmetric situations, have been investigated numerically (Bringedal & Kumar, 2017; Schulz et al., 2017; van Noorden, 2009a). This has led to a greatly simplified set of equations: Instead of the level-set equation, an ordinary differential equation is solved and coupled to the partial differential equations for transport. In Ray, Oberlander, et al. (2019) the fully coupled micro-macro problem in the situation of prescribed velocity was considered. Recently, similar models based on a phase-field formulation have been studied numerically including Darcy flow (Bastidas et al., 2020).

In this paper, we address the numerical investigation of the full problem including both liquid flow and the level-set equation. As a motivation, we study the evolution of and relation between the porosity and reactive surface, also in the situation of a changing topology. Moreover, the permeability is investigated for a microfluidic device similar to Ahkami et al. (2018) as well as for the dissolution of mineral composites adapted from Ellis et al. (2011). We observe that eigenvalues with value zero may become positive in a setup involving topological changes in the microstructure. Ultimately, we investigate the dissolution of an array of dolomite grains similar to Molins et al. (2017), but in the micro-macro context. The evolution and the strong coupling of scales generally necessitates solving as many cell problems as there are elements in the discretization on the macroscale. However, in the situation of a small Péclet or Damköhler number, a drastic reduction in complexity is possible since it then becomes evident that compact or uniform dissolution takes place; see Golfier et al. (2002) for a thorough investigation of dissolution regimes with a focus on wormhole formation and (Battiato et al., 2009, 2011) for a study on the validity of upscaled models in different regimes. For compact dissolution it is reasonable to consider only one representative, but evolving unit cell and corresponding cell problems per vertical slice (cf. Ray, Oberlander, et al., 2019). Another strategy that is applied throughout this research in order to cope with the micro-macro problem's complexity is adaptivity. Here, we aim to minimize the number of evaluations of cell problems, that is, recomputations of effective parameters. To this end, we evaluate how the current geometry deviates from a circular geometry or from previous geometries. These strategies in combination with parallelization lead to weak scalability and result in reasonable computation times.

As discretization methods for the level set, we apply a second order upwind scheme (Sethian, 1998a). EXtended Finite Element Methods are used to evaluate the auxiliary cell problems for the diffusion tensor, whereas adaptive mesh refinement strategies are applied for the Stokes type cell problems. These are discretized with P_2/P_1 elements and solved using a Uzawa type algorithm. For the macroscopic flow and transport equations, Mixed Finite Elements are applied. We quantitatively validate our numerical scheme by providing orders of convergence in the micro and macro discretization parameters and compare our simulation results to the outcome of a pore-scale simulation for the dissolution of an array of dolomite grains. To further prove the applicability of our method, we investigate dissolution in domains with randomly chosen porosity and illustrate the performance of our adaptivity scheme.

Outline: In section 2, a pore-scale model including dissolution reactions and the corresponding micro-macro model are stated. In section 3, the discretization methods and the overall solution strategy are discussed. In section 4, various illustrative examples are numerically investigated to show the importance of an accurate parametrization. Thereafter in section 5, the fully coupled micro-macro problem is investigated with the outcome being evaluated quantitatively.

2. Mathematical Model

In this section, we recapitulate a pore-scale model for mineral dissolution reactions and the corresponding upscaled micro-macro model similar to van Noorden (2009a). For all subsequently introduced quantities the related dimensions are given in terms of length L, time T, and number of particles N. We consider transport and flow in porous media on a rectangular domain $\Omega \subset \mathbb{R}^2$ with boundary $\partial\Omega$. In the context

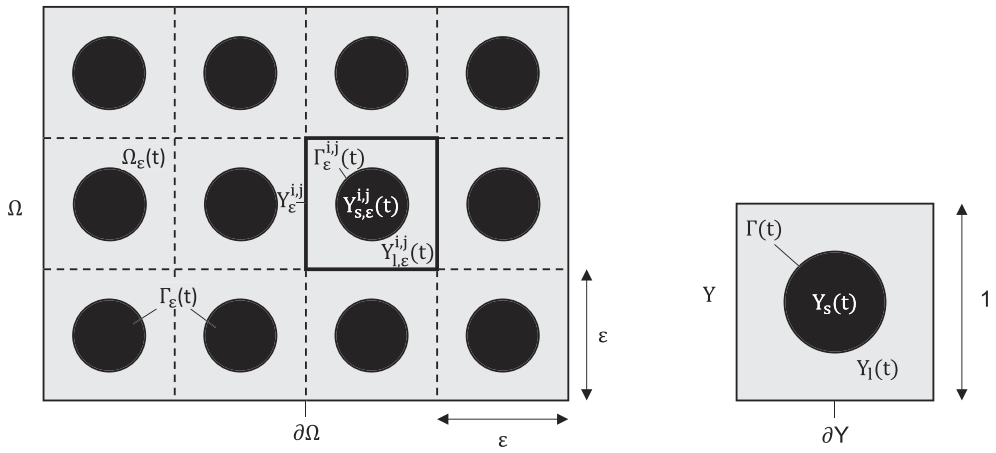

Figure 1. Partition of domain Ω in ε-scaled reference cells. Each of the corresponding unit cells (right) is time dependently decomposed into solid part $Y_s(t)$ and liquid part $Y_l(t)$, separated by interface $\Gamma(t)$. Ω_ε denotes the entirety of all liquid parts in Ω, colored in gray.

of micro-macro simulations, an underlying microstructure is attached to this macroscopic domain in each grid point. Assuming an ideal porous medium, a periodic partition of Ω with ε-scaled unit squares $Y_\varepsilon := \varepsilon Y$ with scale parameter $\varepsilon \ll 1$ is performed. Y is decomposed into a time-dependent solid part $Y_s(t)$ and liquid part $Y_l(t)$. Likewise, each $Y_\varepsilon^{i,j}$ is decomposed into the time-dependent scaled versions $Y_{s,\varepsilon}^{i,j}(t)$ and $Y_{l,\varepsilon}^{i,j}(t)$ with indices $i, j \in \mathbb{N}$ denoting row and column indexes within the regular array; see Figure 1. That is, for all $\varepsilon > 0$

$$Y := \overline{Y_s} \cup \overline{Y_l}, \quad Y = \left[-\frac{1}{2}, \frac{1}{2}\right]^2 \ [\mathrm{L}^2], \quad \Omega = \underset{i,j}{\cup} Y_\varepsilon^{i,j} \ [\mathrm{L}^2], \quad \Omega_\varepsilon := \underset{i,j}{\cup} Y_{l,\varepsilon}^{i,j}.$$

Since chemical reactions take place at the solid surface, the liquid-solid interfaces (interior boundaries) $\Gamma_\varepsilon^{i,j} := \overline{Y_{l,\varepsilon}^{i,j}} \cap \overline{Y_{s,\varepsilon}^{i,j}}$ capture the time evolution of the system. We further denote

$$\Gamma_\varepsilon := \underset{i,j}{\cup} \Gamma_\varepsilon^{i,j} \quad [\mathrm{L}].$$

2.1. Pore-Scale Model

In the following we consider a sequence of problems depending on the scaling parameter ε. Therefore, all occurring quantities are equipped with a subscript ε. In order to deal with time-evolving domains, the level-set method is applied (Osher & Sethian, 1988; Sethian, 1999; Xu et al., 2012). That is, the current domain $\Omega_\varepsilon(t)$ is encoded as the zero sublevel set of a real-valued function $L_\varepsilon : (0,T) \times \Omega \to \mathbb{R}$ [−] defined on a fixed maximal domain Ω. For our setting, we define

$$L_\varepsilon(t,x) = \begin{cases} < 0 & \text{liquid phase/pore space,} \\ = 0 & \text{interface,} \\ > 0 & \text{solid phase.} \end{cases}$$

Solving the level-set equation

$$\begin{aligned} \partial_t L_\varepsilon + v_{n,\varepsilon} |\nabla L_\varepsilon| &= 0, \quad x \in \Omega, \ t \in (0,T), \\ L_\varepsilon(0,\cdot) &= L_\varepsilon^0, \quad x \in \Omega, \end{aligned} \tag{1}$$

with $v_{n,\varepsilon} : (0,T) \times \Omega \to \mathbb{R}$ [LT^{-1}], results in a movement of the interface with speed $v_{n,\varepsilon}$ in normal direction. In the context of geometry changes due to dissolution processes at the interface, it is reasonable to relate $v_{n,\varepsilon}$ to the surface reaction rate f [$\mathrm{N(LT)}^{-1}$] at the interface in a mass conserving way:

$$v_{n,\varepsilon|\Gamma_\varepsilon} = \alpha f\left(c_{|\Gamma_\varepsilon}\right) \quad [\mathrm{LT}^{-1}], \tag{2}$$

with inverse mineral density $\alpha = \frac{1}{\rho}$ [$\mathrm{L}^2\ \mathrm{N}^{-1}$] (Li et al., 2010; van Noorden, 2009a). The fact that $v_{n,\varepsilon}$ must be defined globally on Ω to solve (1) will necessitate the introduction of a suitable extension operator, for example, as proposed in Frolkovič (2012) and Osher and Fedkiw (2006).

Examining again the case of surface reactions with rate f, we consider ε-scaled transport equations for the vector of concentrations c_ε [N L^{-2}] as follows:

$$\begin{aligned} \partial_t c_\varepsilon - \nabla \cdot (-v_\varepsilon c_\varepsilon + D\nabla c_\varepsilon) &= 0, \quad && x \in \Omega_\varepsilon(t),\ t \in (0,T), \\ (-v_\varepsilon c_\varepsilon + D\nabla c_\varepsilon) \cdot \nu_\varepsilon - \varepsilon\alpha f(c_\varepsilon)(c_\varepsilon - \rho) &= 0, \quad && x \in \Gamma_\varepsilon(t),\ t \in (0,T), \\ c_\varepsilon &= c^0, \quad && x \in \Omega_\varepsilon(0), \end{aligned} \tag{3}$$

with molecular diffusion D [L^2 T^{-1}] and outer normal unit vector ν_ε. The scaling with ε is chosen such that $\Gamma_\varepsilon \sim \varepsilon^{-1}$ is balanced and a reasonable velocity limit is obtained (cf. Hornung, 1997; van Noorden, 2009a). The advective velocity field v_ε and its corresponding pressure field p_ε [N T^{-2}] are obtained as the solution of an ε-scaled Stokes problem

$$\begin{aligned} -\varepsilon^2 \mu \Delta v_\varepsilon + \nabla p_\varepsilon &= 0, && x \in \Omega_\varepsilon(t), && t \in (0,T), \\ \nabla \cdot v_\varepsilon &= 0, && x \in \Omega_\varepsilon(t), && t \in (0,T), \\ v_\varepsilon &= v_{n,\varepsilon}\nu_\varepsilon, && x \in \Gamma_\varepsilon(t), && t \in (0,T), \end{aligned}$$

with dynamic viscosity μ [N T^{-1}] and interface normal velocity $v_{n,\varepsilon}$. The condition imposed on $\Gamma_\varepsilon(t)$ corresponds to a no-slip boundary on the time evolving domain. Supplementary exterior boundary conditions for both equations close the model. These will be specified within the scenarios discussed in section 5.

2.2. Micro-Macro Model

The micro-macro model for mineral reactions results as the leading order approximation of the asymptotically expanded pore-scale model (van Noorden, 2009a), that is, in order 0, which is indicated in the following using the subscript $_{\cdot 0}$. In order to additionally account for nonisotropic dissolution processes, we apply the approach from Ray, Oberlander, et al. (2019). More precisely, a modulation of the interface normal velocity is introduced.

The time evolving liquid domain at the microscale is characterized as $Y_{l,0}(t,x) := \{y \in Y\colon L_0(t,x,y) < 0\}$, its solid-liquid interface accordingly as $\Gamma_0(t,x) := \{y \in Y\colon L_0(t,x,y) = 0\}$. L_0 is propagated via the level-set equation

$$\begin{aligned} \partial_t L_0 + v_{n,0}|\nabla_y L_0| &= 0, \quad \text{in } (0,T)\times\Omega\times Y, \\ L_0 &\text{ periodic in } Y, \end{aligned}$$

with normal velocity $v_{n,0}$ defined by

$$v_{n,0}(t,x,y) = \alpha f(c_0(t,x)) \cdot m(\bar{v}_0(t,x),x,y), \tag{4}$$

with leading order macroscopic concentration c_0, averaged advective velocity $\bar{v}_0$, and speed modulation function $m : \mathbb{R}^2 \times \Omega \times Y \to \mathbb{R}^+$ [−]. In order to obtain a mass conserving constitutive law, $m = 1$ poses a natural choice (Bringedal et al., 2016; van Noorden, 2009a). However, this would restrict all considerations to a locally isotropic case. On the contrary, the admission of heuristic functions $m \neq 1$ allows for anisotropic dissolution. Taking the magnitude of the macroscopic velocity field $|\bar{v}_0|$ as well as the angle with respect to the solid surface into account, we use the anisotropic speed modulation function introduced in Ray, Oberlander, et al. (2019):

$$\begin{aligned} m(\bar{v}_0(t,x),x,y) &:= g(\bar{v}_0(t,x)\cdot v_0(y)), \\ g(x) &:= \begin{cases} \exp(-\mu x^2), & x \le 0 \\ (1-\lambda)\exp(-\mu x^2) + \lambda, & x > 0 \end{cases} \end{aligned} \tag{5}$$

with suitable parameters $\mu > 0$ [T^2 L^{-2}], $0 \le \lambda \le 1$ [−], where v_0 again denotes the outer normal vector. For simple geometries the angle is expected to indicate whether a surface point is located in the upstream or downstream regime (magnitude of difference in behavior controlled by λ), while the fluid velocity determines the extent of deviation from uniform dissolution. As μ governs the sensitivity with respect to the angle, both quantities determine the dissolution pattern and are therefore related to the Péclet and Damköhler number. The specific choice of μ, λ ensures the formation of droplet shaped solids, respecting the deviation in ratio of volume and surface compared to the circular case. Throughout this paper values of $\lambda = 0.75$ and $\mu = 5{,}000$ s^2 dm^{-2} are used as they reproduce the typical shape evolution of a circular grain known from microscopic simulations (Molins et al., 2017; Ray, Oberlander, et al., 2019) in a reasonable range of reactive transport regimes.

The transport equations for the species' concentrations c_0 read

$$\partial_t(\phi c_0) + \nabla_x \cdot (\bar{v}_0 c_0) - \nabla_x \cdot (\mathbb{D}\nabla c_0) = -\sigma f(c_0) \quad \text{in } (0,T)\times\Omega, \tag{6}$$

with porosity ϕ and specific surface σ naturally given by

$$\phi = \frac{|Y_{l,0}|}{|Y|}\ [-], \quad \sigma = \frac{|\Gamma_0|}{|Y|}\ [\mathrm{L}^{-1}]$$

and effective diffusion tensor $\mathbb{D}$ [$\mathrm{L}^2\ \mathrm{T}^{-1}$] given below. Note that the leading order term in the concentrations' expansion c_0 does not depend on y due to standard upscaling results (Hornung, 1997; van Noorden, 2009a).

The averaged velocity field $\bar{v}_0$ [$\mathrm{L}\ \mathrm{T}^{-1}$] is obtained from Darcy's law

$$\begin{aligned} \bar{v}_0 &= -\frac{\mathbb{K}}{\mu}\nabla p_0 && \text{in } \Omega,\ t\in(0,T),\\ \nabla\cdot\bar{v}_0 &= 0 && \text{in } \Omega,\ t\in(0,T),\\ \int_\Omega p_0\,dx &= 0, \end{aligned} \tag{7}$$

with permeability tensor $\mathbb{K}$ [L^2] and macroscopic pressure field p_0 [$\mathrm{N}\ \mathrm{T}^{-2}$]. Requesting vanishing mean pressure leads to a uniquely solvable system. Note that $\bar{v}_0$ is set to be divergence free as opposed to van Noorden (2009a) since the time scale of porosity changes is orders of magnitude larger than that of the fluid flow. Therefore, this quasistatic approximation does not impair accuracy but facilitates simulations. Diffusion and permeability tensor are defined via solutions of standard auxiliary cell problems as follows (Hornung, 1997; van Noorden, 2009a).

Diffusion tensor: $\mathbb{D}_{i,j}(t,x) := \int_{Y_{l,0}(t,x)} D\left(\partial_{y_i}\zeta_j + \delta_{ij}\right)\,dy$ for $i,j\in\{1,2\}$, where ζ_j are the solutions to

$$\begin{aligned} -\nabla_y\cdot(\nabla_y\zeta_j) &= 0 && \text{in } Y_{l,0}(t,x),\\ \nabla_y\zeta_j\cdot\nu_0 &= -e_j\cdot\nu_0 && \text{on } \Gamma_0(t,x),\\ \zeta_j \text{ periodic in } y,\quad \int_{Y_{l,0}}\zeta_j\,dy &= 0, \end{aligned} \tag{8}$$

e_i denoting the ith canonical vector and δ_{ij} the Kronecker delta.

Permeability tensor: $\mathbb{K}_{i,j}(t,x) := \int_{Y_{l,0}(t,x)}\omega_j^i\,dy$ for $i,j\in\{1,2\}$, where (ω_j,π_j) are the solutions to

$$\begin{aligned} -\Delta_y\omega_j + \nabla_y\pi_j &= e_j && \text{in } Y_{l,0}(t,x),\\ \nabla_y\cdot\omega_j &= 0 && \text{in } Y_{l,0}(t,x),\\ \omega_j &= 0 && \text{on } \Gamma_0(t,x),\\ \omega_j,\ \pi_j \text{ periodic in } y,\quad \int_{Y_{l,0}}\pi_j\,dy &= 0. \end{aligned} \tag{9}$$

Again, the mean values are set to zero to ensure the unique solvability of the systems.

3. Numerical Methods

3.1. General Approach

A simple operator splitting approach between microscale and macroscale allows connecting transport/flow solvers with the cell problem solvers via a bidirectional transfer of input data. Such methods are commonly used in multiscale simulations (Bastidas et al., 2020; Ray, Oberlander, et al., 2019). A graphical representation of our complete algorithm is presented in Figure 2 (cf. Ray, Oberlander, et al., 2019). As discussed in section 3.4.2, our adaptivity scheme can partially circumvent an update of the evolution operator associated with the microscale. One cycle in the diagram can correspond to a whole macroscopic time step. As part of an interior fixed-point iteration, also, multiple cycles per time step may be taken.

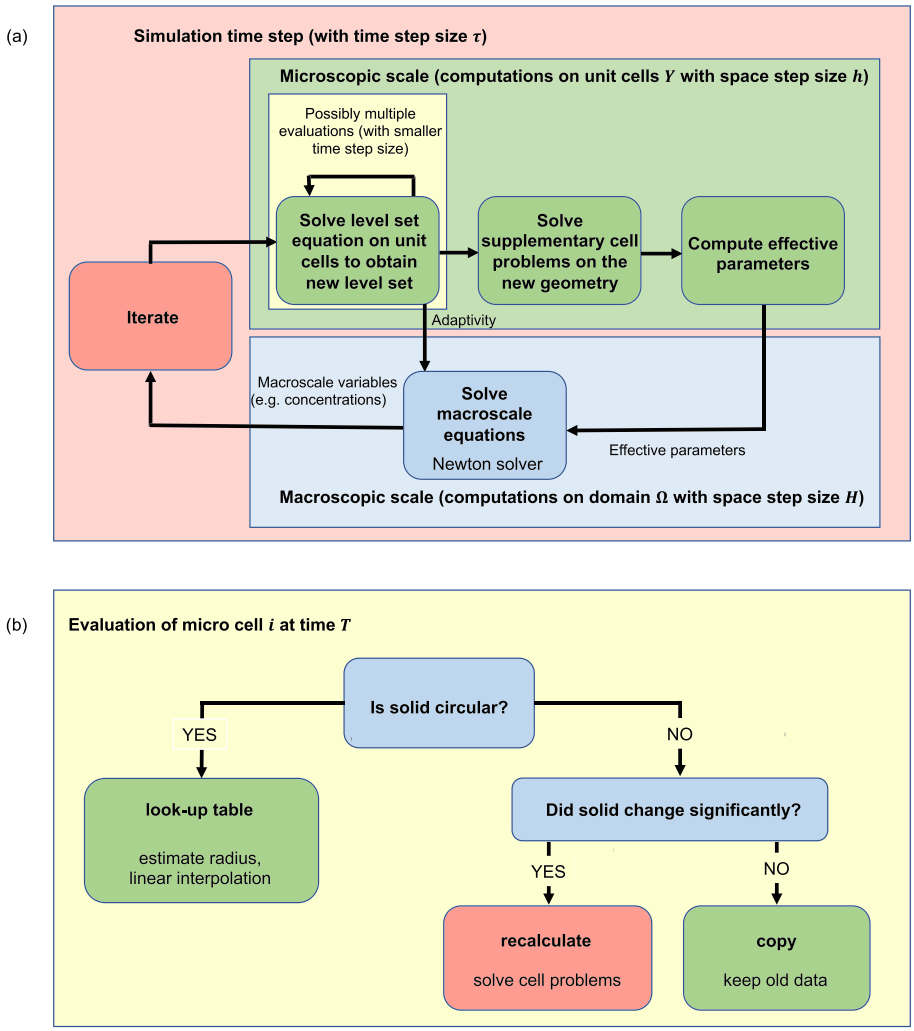

Figure 2. Overall solution algorithm showing operator splitting among bidirectionally coupled scales (a). Adaptivity may partially circumvent the solution of the cell problems (8) and (9). Image (b) displays the principles of the adaptivity scheme minimizing the number of cell problems completely reevaluated. Green exits indicate a subordinate computation time.

In the extreme case of a unit cell being attached to each macroscopic finite element (Figure 3a), the presented method is still practically not feasible due to the enormous overhead. An apparent remedy is the parallelization of the evaluation of the cell problems (8) and (9) as applied in Bastidas et al. (2020). Since these operations can be performed independently of each other, weak scalability is expected and observed; see section 5.

3.2. Discretization of Macroscopic Equations

As one major advantage of our micro-macro approach, the whole time dependency of the computational domain is reflected within the cell problems, whereas flow and transport equations are to be solved on the fixed macroscopic domain Ω . Therefore, we can deploy standard transport solvers, such as included in the MATLAB©Toolbox HyPHM (Frank, 2014). All implementations in this paper are based on MATLAB©Version R2019a (MATLAB, 2019) and the framework of HyPHM, a flexible numerical toolbox for flow and transport simulations. Its problem class "transport" comprises an implementation of mixed finite elements with lowest order Raviart-Thomas elements RT_0 on 2-D triangular unstructured grids and allows for time- and space-dependent coefficient functions. The package routines are coupled to a Newton solver to treat several nonlinearly coupled equations with implicit Euler time stepping. HyPHM is able to handle both types of macroscopic equations—Darcy—and transport equation(s)—in a similar and compatible way.

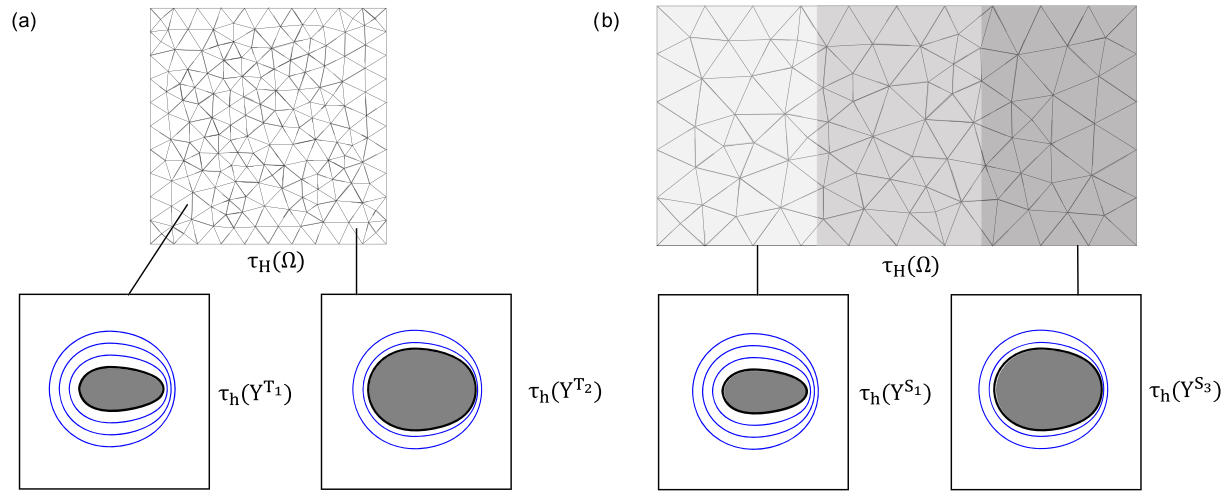

Figure 3. Different possibilities of matching cell problems to macroscopic domain. (a) Macroscopic triangulation $\tau_H(\Omega)$: A microcell Y^{T_i} is attached to each element T_i (general approach). (b) Macroscopic triangulation $\tau_H(\Omega)$: A microcell Y^{S_i} is attached to each vertical stripe S_i (effectively one-dimensional situation; cf. section 5).

This software has already been used successfully in simulations of micro-macro problems (see Frank, 2013; Ray, Oberlander, et al., 2019).

Due to the full coupling of the transport processes in (6) via nonlinear right hand sides, the system matrices arising in every step of Newton's iteration are large in size, badly conditioned and show a complex sparsity pattern. Therefore, iterative solvers with powerful preconditioners are needed. We choose the MATLAB© compatible library *ilupack* (Bollhöfer & Saad, 2006) for this purpose, providing reordering and rescaling routines as well as multilevel ILU decomposition templates and a variety of Krylov subspace methods. In the literature many different methods for efficiently solving the arising sequence of linear systems are discussed (e.g., in Duintjer Tebbens & Tůma, 2007). As the system matrix varies only a little during one call of the Newton solver, we apply the common method of *freezing* the preconditioner of the first iteration in combination with GMRES. In this sense, we trade the quality of all subsequent preconditioners against a possibly higher number of Krylov steps. Since Newton's algorithm involves some robustness, only weak tolerances must be met for the residuals of the linear systems. This allows an efficient distribution of computation time among the sequence of similar systems.

3.3. Level-Set Evolution

Since the solution of the level-set equation is nothing but an auxiliary construct to implicitly encode the current domain within each unit cell, an efficient treatment is desirable. As the cell problems are defined on a unit square, an explicit finite difference scheme on a structured grid with mesh parameter h is appropriate. However, standard finite differences are known to cause spurious behavior due to the advective nature of the level-set equation. In an earlier paper (Ray, Oberlander, et al., 2019), a first-order upwind scheme introduced by Rouy and Tourin (1992) was applied to ensure stability in this context. However, this approach might lead to unsatisfying accuracy.

By construction, the normal velocity field $v_{n,0}$ defined in Equation 4 is continuous and piecewise smooth. We exploit that fact by using a second-order discretization for the spatial gradient as stated in Sethian (1998a). Therefore, not only a more accurate prediction of the volume of the cell's solid is to be expected but also a precise representation of its shape. In Figure 4, an initial circle (green) is contracted by prescribing a uniform interface velocity, and first- and second-order schemes are compared. The zoom-in version on the right visualizes the aforementioned differences. As elaborated in Ray et al. (2018) and Schulz et al. (2019), both properties—volume and shape—have a significant influence on permeability and diffusivity. Although the higher-order correction increases the computational effort by a factor of approximately 3, the total computation time of the level-set solver is still almost negligible; see Figure 10. Furthermore, an increased order of convergence is observed for subsequent calculations performed on the geometry (cf. section 5).

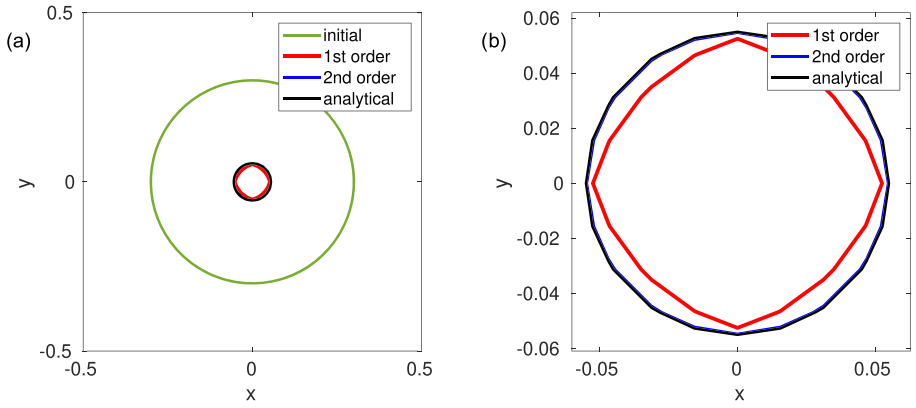

Figure 4. Uniform contraction of a circle via constant normal velocity v_n. Comparison of different order upwind schemes against the analytical solution, showing shape preserving property of second-order method after the same number of time steps. Right image depicts a magnification of the center of contraction.

Consequently, we apply a second-order scheme in this research when normal velocities are sufficiently smooth.

Let $(D_{\pm i})^k$ denote the usual forward/backward difference quotient of order k along the i axis and L_{ij}^n the approximation of the level set at grid point $\{i,j\}$ and time step n. Then, in two dimensions the second-order upwind scheme is written as

$$L_{ij}^{n+1} = L_{ij}^n - \tau \left(\max\{v_{n,0}, 0\} \nabla^+ + \min\{v_{n,0}, 0\} \nabla^- \right)$$

with time step size $\tau > 0$; see Sethian (1998b). $\nabla^{\pm}$ denotes the part of the discretization of the spatial gradient related to the upwind and downwind regime (in relation to a positive interface velocity), respectively. The scheme involves information arriving from the direction of the source. See Gärttner et al. (2020) and Sethian (1999) for further details. A standard CFL-condition of the form

$$\tau \leq C \frac{h}{\max |v_{n,0}|}, \quad C > 0,$$

yields a stable and efficient second-order algorithm. All operations are implemented in a fully vectorized manner.

3.4. Discretization and Adaptivity of Cell Problems

3.4.1. Discretization of Cell Problems

As elaborated in the last section, the level-set approach allows a convenient implicit representation of the time-dependent liquid-solid interface $\Gamma_0(t)$. For the purpose of extracting properties from the underlying microstructure, these interfaces within the cells must be handled properly. The calculation of porosity and specific surface can easily be performed using a piecewise linear reconstruction of $\Gamma_0(t)$. As discussed in section 2.2, the effective diffusion and permeability tensors are determined from solutions of the auxiliary cell problems (8) and (9). For the treatment of the diffusion tensor defined via the solution of Equation 8, we maintain our EXtended Finite Elements (XFEM) scheme on a Friedrichs-Keller triangulation as presented in Ray, Oberlander, et al. (2019). This allows using the same nodal points for the level-set evolution as well as for the elliptic diffusion problems, since the entire geometric information of the cell domains $Y_{l,0}$ is processed within the matrix assembly. In particular, the total number of degrees of freedom is small and not varying over time. The final construction of the diffusion tensor requires an integration of the fluxes of the PDEs' solutions. To do so, numerical differentiation is inevitable in our framework, bearing the danger of inaccurate results. We investigated this threat by means of a comparison to a mixed finite element approach on an accordingly refined mesh. For our purposes, the observed gain in accuracy could not compensate the increase of computation time.

In order to calculate the permeability tensor from the geometry within the unit cells, one stationary Stokes problem per dimension, that is, two in 2-D, must be computed. We use a stable P_2/P_1 discretization for the velocity and pressure space and impose zero Dirichlet boundary conditions for the velocity at the solid-liquid

interface. The computational efficiency of our Stokes solver is based on a fully vectorized system assembly (see Japhet et al., 2013) and the application of Uzawa's algorithm, a linear solver specifically tailored for saddle point problems of the form $S = \begin{pmatrix} A & -B^T \\ -B & 0 \end{pmatrix}$; see Koko (2019). Within this iterative scheme, the pivotal operation is the solution of the linear subsystem A—originating from the Laplace-part of the equation—with changing right-hand sides. We therefore precompute a Cholesky decomposition of A, basically reducing the computational effort of each iteration to substitution operations. In order to improve convergence, the pressure part B is preconditioned by a diagonal matrix derived from the mass matrix to counteract different scaling behavior of the entries in the microscopic mesh parameter h. Since the permeability is very sensitive to geometrical changes, properly accounting for the current interface position is crucial; see illustrations in Figures 7 and 8. In settings where the interface is not tracked precisely, as it is usually the case for diffuse interface models, predicted permeabilities tend to be inaccurate (Bringedal et al., 2019).

Unfortunately, the enrichment of the velocity field with appropriated cut-off functions—as usually performed in the scope of XFEM methods—is known to suffer from stability issues and poor accuracy improvements (Sauerland, 2013). Therefore, local mesh refinement strategies in the proximity of the interface are deployed. Adapting the scheme presented in Li and Song (2012) to our FEM framework, a first-order refinement algorithm is applied.

More precisely, we use a linear interpolation of the level-set values at the nodal points L^n_{ij} along the edges of each triangle and possibly add the zeros as new points to the interface. Again, for sake of stability, this procedure includes a regularization parameter. If a new point is closer to an already existing one in the grid than the prescribed threshold, it will be disregarded. Instead, this neighbor is set to be a root of the level set. Thereby, mesh regularity is maintained preserving numerical stability. Special attention must be paid at the refinement along the exterior boundary ∂Y due to the periodic boundary conditions (Kim & Swan, 2003). We therefore deactivate the mesh adjustments along ∂Y to avoid impairment of the folding procedure. Application of a standard Delaunay triangulation algorithm restores the Friedrichs-Keller triangulation away from the interface and ensures a globally conforming grid.

3.4.2. Adaptivity

In the context of adaptive numerical homogenization and heterogeneous micro-macro methods (HMM), adaptive methods are often based on a posteriori error indicators; see, for example, Bastidas et al. (2019). These may in general decide about local refinement or coarsening of the discretization, control the size of the domain where microscale simulations are performed, or include any kind of learning algorithm (Bastidas et al., 2019; Redeker, 2014; Redeker & Eck, 2013; Weinan et al., 2007).

For realistic applications including many cell problems, such as investigated in section 5, a minimization of the number of cell problems' reevaluation is crucial. We adapt the scheme presented in Redeker and Eck (2013); see Figure 2b. The approach relies on the assumption that similar input data to the cell problems lead to similar output data. Although sharp estimates of the error amplification are usually unavailable, the degree of uncertainty of the input data is a useful indicator for whether a recalculation will increase the quality of the output data. Our specific criterion is presented later in this section. In Redeker and Eck (2013), the adaptive strategy is based on the input data arising from the evolution of the macroscopic fields. In our framework, the back coupling from the macroscale to the microscale is realized by the prescription of the normal interface velocity via (4). Since the evolution of the level set is of subordinate complexity, information about the magnitude of evolution as well as the current microgeometry is available at any time. We therefore base our adaptivity scheme directly on the level-set function.

Diffusion and permeability are expected to depend continuously on the solid part $Y_{s,0}$. In order to avoid the effort of calculating local error estimates, we exploit the directly accessible information about the extent of microscopic evolution. Evaluation of the expression $\sup_{y\in Y}\{|v_{n,0}|\}\cdot\tau$ with macroscopic time step size τ allows estimating the magnitude of alternation taken place since the last macroscopic time step. If the expected changes from the previous geometry are small, we reuse the old data without performing a reevaluation. In order to preserve the desired level of accuracy, the quantity,

$$\sum_{i=j}^{k} \sup_{y\in Y}\{|v_{n,0}(t=t_i)|\}\cdot\tau(t=t_i),$$

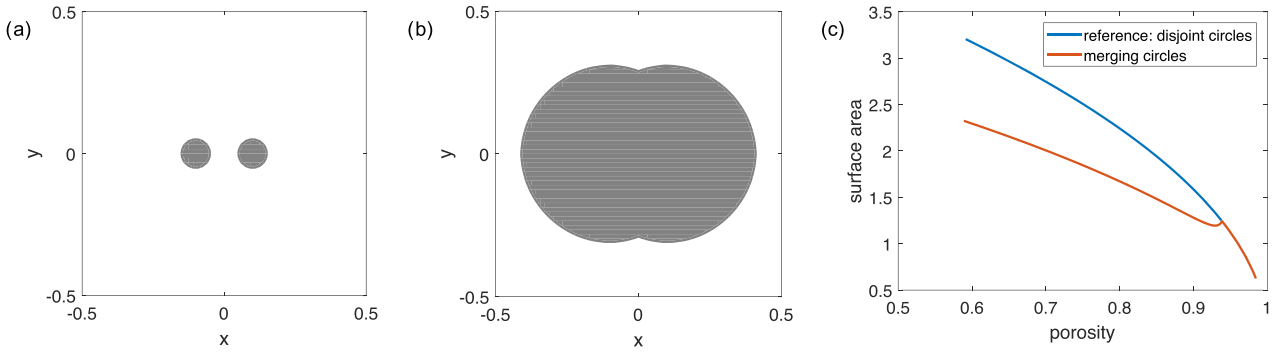

Figure 5. Dependence of specific surface area σ [L^{-1}] on porosity ϕ for two different geometrical settings illustrating the impact of topological changes. Initial (a) and final (b) geometry in the merging circles scenario are depicted, as well as the actual specific surface area—porosity relation (red) in comparison to a standard power law (blue) (c).

where t_k denotes the current discrete time and t_j the time of last reevaluation of the respective cell, should be small. More precisely, we do not consider variations of the input data far below the discretization parameter h since no gain in accuracy of the output data can be expected from such variations. This is due to the fact that the discretization errors limit the accuracy. Likewise, the uncertainty of measurements or input data with restricted spatial resolution (directly relating to the discretization parameter h), for example, from voxelized CT data, leads to a restriction in accuracy. In the experiment conducted in section 5.3, the threshold is set to 20% of the mesh parameter. This procedure can be interpreted as a spatially local coarsening of the microscopic time discretization. The approach presented allows focusing computation power to the subdomains of Ω experiencing pertinent changes of the underlying microstructure.

Additionally, another strategy is implemented to possibly reduce the number of cell problems evaluated in highly symmetrical scenarios. After initializing the solid part of the cell domains $Y_{s,0}$ as circular, the circular shape is approximately preserved over a certain time interval. Therefore, we treat these situations separately by checking for this property in advance, using methods known from data analysis (Sehgal et al., 2014). More precisely, we use a linear interpolation of the level set and sample the solid part on a refined mesh. The resulting point cloud is then used to check for symmetry properties and approximate the center of mass position as well as a possible radius. In case of a circular solid, we use that information to calculate the associated diffusion and permeability tensors from a linear interpolation of look-up tables as suggested in Frank (2013). Alternatively, analytical expressions linking porosity to these quantities can be deployed; see Ray et al. (2018) and Schulz et al. (2019). In the case of a unit cell containing an approximate circular shape, our tests show the time for shape detection and tensor evaluation to be less than 1% compared to solving the cell problems. This part of our adaptivity approach can be understood as an a priori learning method.

4. Simulations of Hydraulic Parameters

In this section, we present some test problems for the calculation of the effective parameters from the level-set function used later in the micro-macro simulation. The impact of varying diffusion tensors on the macroscopic solution and its dependence on pore-scale geometry has been discussed extensively in Ray, Oberlander, et al. (2019). We will therefore illustrate the relation between topological changes at the microlevel and the reactive surface area as well as evolving permeability tensors.

4.1. Porosity and Surface Area

Considering the reactive transport equation given in (6), it is evident that the specific surface area σ controls the strength of the source term. Whereas the evolution of the porosity ϕ in time can easily be deduced from the local mass conservation property of the transport equation (and its discretization for RT_0/P_0 elements), the specific surface area is a quantity generally not accessible from macroscopic information. As a remedy, the following relation between σ and ϕ is often assumed in three dimensions (Seigneur et al., 2019):

$$\sigma = \sigma_0 \left(\frac{1-\phi}{1-\phi_0} \right)^{\frac{2}{3}},$$

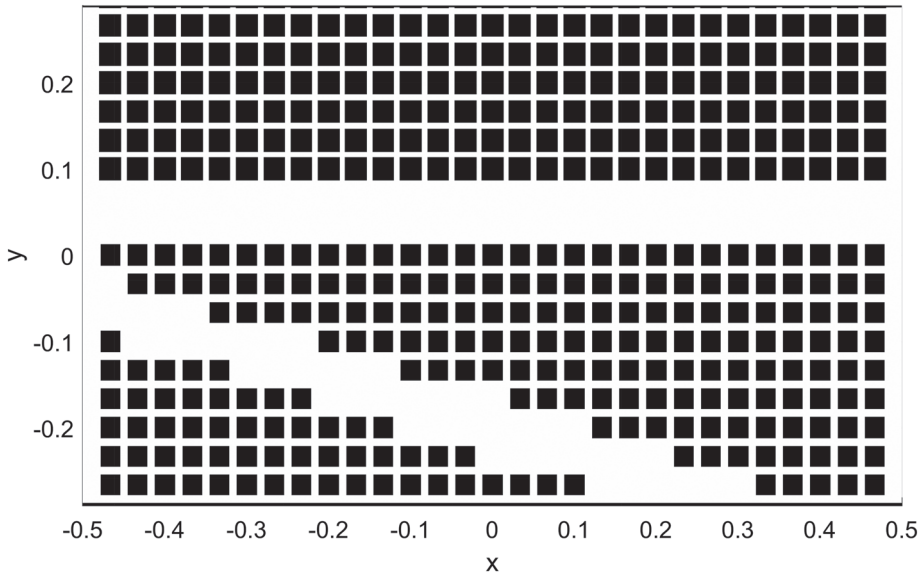

Figure 6. Binary porosity map characterizing the geometry of a microfluidic device. Porous matrix within the flow channel consisting of square-shaped solids. The upper matrix exhibits a porosity of 0.21, the lower one of 0.29.

with reference surface area σ_0 at ϕ_0. In our two-dimensional setup this transfers to $\sigma = \sqrt{4\pi(1-\phi)}$ for circular grains. In contrast, with our level-set approach we are able to calculate the (specific) surface explicitly based on the underlying reactive processes. To illustrate the order of magnitude the heuristic law deviates from the real porosity, (specific) surface relation in scenarios involving topological changes of the solid domain Y_s, we consider the merging of two circles; see Figure 5. In application, this situation may for instance occur due to substantial precipitation. We position two circles of radius 0.05 at a distance of 0.2 and let the interface evolve in normal direction with unit speed. By a linear reconstruction of the level-set function on each triangle of the underlying discretization, both ϕ and σ are easily determined. In Figure 5c, the resulting relation between both quantities is depicted (red line). As a reference, the corresponding relation without changes in topology $\sigma = \sqrt{8\pi(1-\phi)}$ is displayed as well (blue line). The critical porosity $\phi_{crit} = 1 - \frac{\pi}{50} \approx 0.9372$, that is, when the two circles touch each other in a single point, is clearly visible as a kink in Figure 5c. More precisely, monotonicity behavior is inverted locally at the critical value. For low porosities, both graphs differ by a factor of $\sqrt{2}$. We therefore expect reaction properties to change dramatically under exchange of the aforementioned cell geometries. Due to this strong impact, it is essential to include a detailed description of the ϕ-σ relation for accurate modeling, which is easily possible in the level-set context. The same reasoning immediately translates into the poor approximation capabilities of similar power laws approximating diffusivity and permeability for such scenarios (cf. Figure 7). This justifies the computational effort invested in geometry evolution and evaluation by our approach.

4.2. Permeability Tensors

In order to evaluate the quality of the permeability solver described in section 3.4.1, quantitative comparisons have been rendered against the literature (see Frank, 2013; Guibert et al., 2016; Sobera & Kleijn, 2006). Moreover, we validated translational invariance arising from the periodic boundary conditions. Note that all shapes are defined via suitable level-set functions on a fixed grid.

First, to underline the flexibility of our algorithm, we calculate the permeability of a microfluidic device. Similar to the setup presented in Ahkami et al. (2018), we consider a two-dimensional device hosting a fractured porous medium with an inlet at the left end. More precisely, one horizontal fracture in the direction of main flow separates two porous matrices of porosity 0.21 (upper) and 0.29 (lower), consisting of square-shaped inclusions. Additionally, another diagonal fracture is embedded into the lighter matrix. The porosity map describing this complex geometry is depicted in Figure 6.

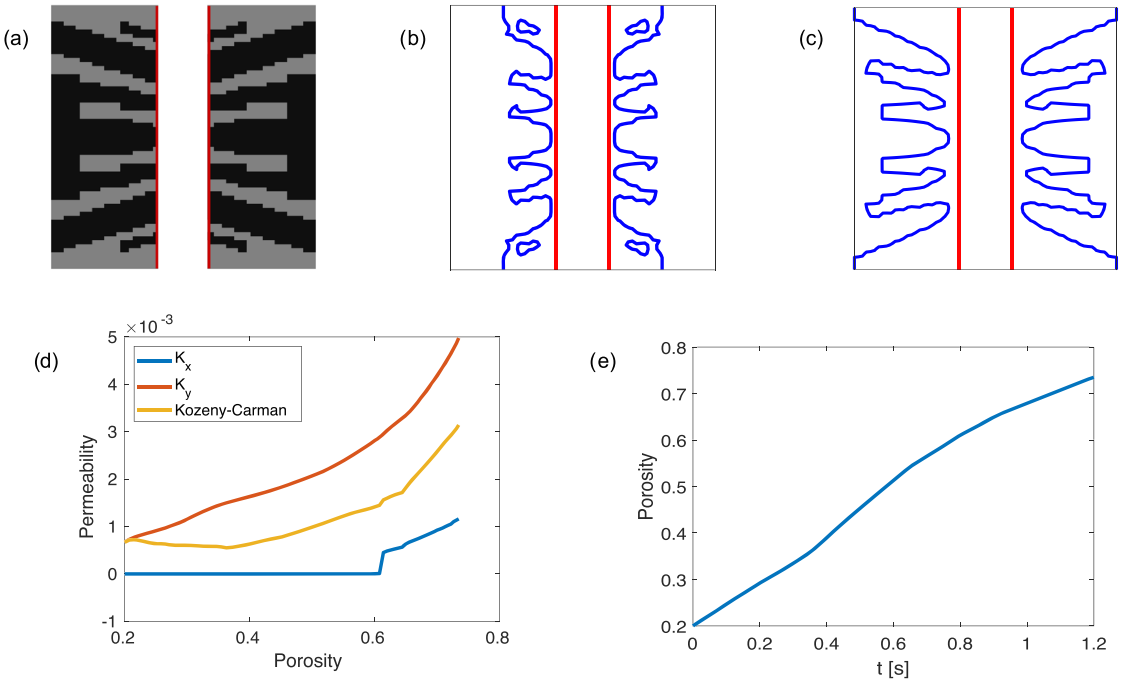

Figure 7. Dissolution of a composite material and simultaneously calculated permeability. The initial configuration is shown in (a), consisting of calcite (gray) and dolomite (black). For $T = 0.4$ s and $T = 0.8$ s the current interface is depicted in blue, the initial configuration in red (b, c). The bottom row shows the diagonal components of the associated permeability tensor in comparison to Kozeny-Carman (d) as well as the porosity evolution (e) over time.

Calculations on a regular 1,000 × 1,000 grid predict a permeability of

$$\mathbb{K} = 10^{-5} \cdot \begin{pmatrix} 3.870 & 0.000 \\ 0.000 & 0.000 \end{pmatrix} \quad [\mathrm{L}^2].$$

As expected, the setup is only permeable along the x axis while all other entries of the tensor are at least 8 orders of magnitude smaller in modulus.

Second, in order to test the interplay of permeability, and level-set solver, we investigate the dissolution of a composite material in generalization of Molins et al. (2017) and Ray, Oberlander, et al. (2019); see Figure 7. In this scenario, two different dissolving materials are considered with interface velocities differing by a factor of 10 (Figure 7a). Starting from a central channel at time $T = 0$, both materials are dissolving with their respective speeds in normal direction and the current interface between the materials, and the void space is traced (cf. Figures 7b and 7c). For every evolution step of the level set a recalculation of the permeability tensor is implemented (Figure 7d). We also compared the results to a standard Kozeny-Carman power law of the type (Schulz et al., 2019)

$$K = \frac{c_0}{\sigma_{SV}} \frac{\phi^3}{(1-\phi)^2},$$

where σ_{SV} $[\mathrm{L}^{-1}]$ denotes the specific surface with respect to the unit volume of the solid part and c_0 is a geometry dependent constant. All calculations were performed on a regular 64 × 64 grid.

The permeability in y direction increases over time whereas the configuration remains impermeable in x direction for small times T. After about 0.8 s, the wormholes are formed. Accordingly, a permeability tensor with two positive eigenvalues is obtained. However, such rapid structural changes are not displayed using the Kozeny-Carman relation; see Figure 7d. As the permeability tensor enters Darcy's equation (7), deviations in $\mathbb{K}$ have direct impact on the macroscopic flow field.

In a last example, we present an application that couples our permeability solver to reactive transport. Inside the square $[0, 0.1]^2$ $[\mathrm{dm}]^2$, a circle of radius 0.03 dm is considered, being horizontally subdivided into two semicircles. Each of them is composed of a different mineral (e.g., calcite and dolomite) with different

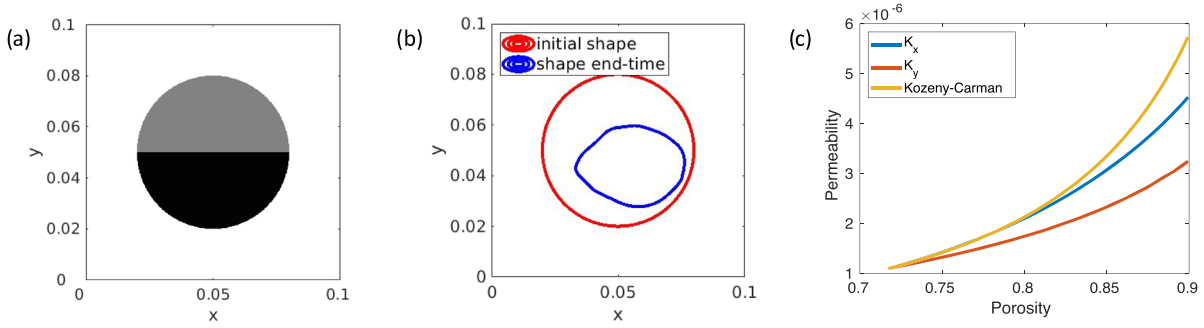

Figure 8. Calculation of permeability tensors on an evolving domain. A circle of composite mineral (a) is dissolved in a microscopic reactive transport simulation, causing anisotropic shape deformation (b). The evolution of the related permeability tensor [m^2] is depicted in (c).

reaction pathways and dissolution speeds; see Figure 8a. The dolomite part dissolves via the equation presented in section 5, the calcite part according to Ray, Oberlander, et al. (2019):

$$r_m = \left(k_1 c_{\mathrm{H}^+} + k_3\right)\left(1 - \frac{c_{\mathrm{Ca}^{2+}} c_{\mathrm{CO}_3^{2-}}}{K_{\mathrm{s,cal}}}\right), \quad \vec{R}_{\mathrm{cal}}(\vec{c}) = \begin{pmatrix} -k_1 c_{\mathrm{H}^+}\left(1 - \frac{c_{\mathrm{Ca}^{2+}} c_{\mathrm{CO}_3^{2-}}}{K_{\mathrm{s,cal}}}\right) \\ r_m \\ r_m \end{pmatrix}$$

with $k_1 = 0.89\,[\mathrm{mol\,m^{-1}\,s^{-1}}]$, $k_3 = 6.6 \cdot 10^{-7}[\mathrm{mol\,m^{-1}\,s^{-1}}]$, $K_{\mathrm{s,cal}} = 10^{-8.234}$, and $\vec{c} = \left(c_{\mathrm{H}^+}, c_{\mathrm{Ca}^{2+}}, c_{\mathrm{CO}_3^{2-}}\right)^T$. The shape development of the solid-liquid interface depicted in Figure 8b stems from an actual microsimulation including reactive flow. Since the solid part will not preserve its symmetry, we expect the permeability tensor to become gradually more anisotropic. Its dependence on the porosity is also depicted in Figure 8c. For comparison, the Kozeny-Carman approximation is plotted as well, being scaled to fit the calculation at the initial geometry. As it is evident from our results, the Kozeny-Carman relation cannot yield an accurate description since it cannot capture the anisotropic behavior simultaneously in both spatial directions.

5. Micro-Macro Simulations

We now apply our fully coupled micro-macro approach to the dissolution of dolomite. More precisely, the reaction path

$$\mathrm{CaMg}(CO_3)_2 \rightleftharpoons Ca^{2+} + Mg^{2+} + 2CO_3^{2-}$$

with rate

$$r_m = k a_{\mathrm{H}^+}^{0.5}\left(1 - \frac{a_{\mathrm{Ca}^{2+}} a_{\mathrm{Mg}^{2+}} a_{\mathrm{CO}_3^{2-}}^2}{\mathrm{K}_{s,dol}}\right)$$

as used in Molins et al. (2017) is considered. Equilibrium constant $K_{\mathrm{s,dol}}$ and rate coefficient k are set to

$$K_{\mathrm{s,dol}} = 10^{-16.5}, \quad k = 4.5 \cdot 10^{-4}\ \mathrm{mol\,m^{-1}s^{-1}}.$$

See Michaowski and Garcia Asuero (2012) and Molins et al. (2017). For simplicity, we regard concentration c and activity a of the chemical species as identical in value, dropping units. Denoting the vector of solutes' concentrations by $\vec{c} = \left(c_{\mathrm{Ca}^{2+}}, c_{\mathrm{Mg}^{2+}}, c_{\mathrm{CO}_3^{2-}}, c_{\mathrm{H}^+}\right)^T$, the complete reaction vector is given by

$$\vec{R}(\vec{c}) = \begin{pmatrix} r_m \\ r_m \\ 2r_m \\ 0 \end{pmatrix}$$

according to the stoichiometric coefficients. On the rectangular domain $\Omega = [0,1] \times [0,0.5]$ [cm^2] we consider the following macroscopic transport equations and boundary/initial conditions adopted from Ray, Oberlander, et al. (2019):

$$
\begin{aligned}
\partial_t(\phi \vec{c}) + \mathcal{L}\vec{c} &= \frac{1}{\varepsilon}\sigma \vec{R}(\vec{c}) \quad \text{in } (0,T)\times\Omega,\\
\left(\mathcal{L}\vec{c}\right) &:= \nabla \cdot \left(\vec{c} \otimes \vec{v} - \mathbb{D}\nabla \vec{c}\right),\\
(c_* \vec{v} - \mathbb{D}\nabla c_*)\cdot \nu &= 0 \quad \text{on } (0,T)\times\Gamma_{\pm},\\
* &\in \{Ca^{2+}, Mg^{2+}, CO_3^{2-}, H^+\},\\
(c_\dagger \vec{v} - \mathbb{D}\nabla c_\dagger)\cdot \nu &= 0 \quad \text{on } (0,T)\times\Gamma_{\text{in}},\\
\dagger &\in \{Ca^{2+}, Mg^{2+}, CO_3^{2-}\},\\
(c_{H^+} \vec{v} - \mathbb{D}\nabla c_{H^+})\cdot \nu &= 10^{-5}\vec{v}\cdot\nu \quad \text{on } (0,T)\times\Gamma_{\text{in}},\\
-\mathbb{D}\nabla c_* \cdot \nu &= 0 \quad \text{on } (0,T)\times\Gamma_{\text{out}},\\
c_\dagger(0,\cdot) &= 0 \quad \text{in } \Omega,\\
c_{H^+}(0,\cdot) &= 10^{-5}\ [\text{mol dm}^{-2}] \quad \text{in } \Omega,
\end{aligned}
$$

with $\Gamma_{\text{in}} = \{0\}\times(0,0.5)$ (left), $\Gamma_{\text{out}} = \{1\}\times(0,0.5)$ (right), $\Gamma_{\pm} = (0,0.5)\times\{0,1\}$ (top/bottom). These equations model the injection of an acidic solution at pH 5 from the left boundary. While no-flux conditions are posed at the upper and lower boundary for all species, the right edge corresponds to an outflow boundary.

Instead of an artificially prescribed advective velocity field $\vec{v}$ as in Ray, Oberlander, et al. (2019), we solve Darcy's equation

$$
\begin{aligned}
\vec{v} &= -\frac{\mathbb{K}}{\mu}\nabla p && \text{in } \Omega,\ t \in (0,T),\\
\nabla\cdot\vec{v} &= 0 && \text{in } \Omega,\ t \in (0,T),\\
\vec{v}\cdot\nu &= -10^{-2} \text{ or } -10^{-1}\ \text{[cm/s]} && \text{on } \Gamma_{\text{in}},\ t \in (0,T),\\
\vec{v}\cdot\nu &= 0 && \text{on } \Gamma_{\pm},\ t \in (0,T),\\
p &= 0 && \text{on } \Gamma_{\text{out}},\ t \in (0,T).
\end{aligned}
$$

Accordingly, the system is driven by an inflow over the left boundary Γ_{in}. The obtained velocities correspond to Péclet numbers 500 or 5,000, respectively. Diffusion coefficient and dynamic viscosity are set to $D = 2\cdot 10^{-9}$ m^2 s^{-1} and $\mu = 1.1\cdot 10^{-3}$ kg s^{-1}, respectively (Rumble, 2018; Wang, 1965). As discussed in section 2.2, the normal interface velocity takes the form $v_n = \varepsilon^{-1} V_m r_m(\vec{c})\cdot m$ with speed modulation function m defined in (5) and molar volume $V_m = 6.412\cdot 10^{-2}$ dm^2 mol^{-1} (WWW-MINCRYST, 2014). Additionally, level set and cell problems as formulated in section 2 supplement the model.

5.1. Choice of Discretization Parameters and Convergence Studies

Our solution algorithm for micro-macro models presented in section 3.1 leaves the choice of two mesh parameters h and H. The microscopic parameter h determines the fineness of the grids within each unit cell Y; the macroscopic parameter H prescribes the fineness of the discretization of Ω as a fraction of the domain's extent in x direction. As the microscopic model part only delivers auxiliary information to the macro problem, its share of computational time should be rather small. Nevertheless, convergence to the continuous solution can only be expected for $h, H \to 0$. We therefore discuss reasonable choices for the relation between h, H in order to satisfy both requirements in terms of efficiency and accuracy.

First, a simplified setting with only one single cell encoding the underlying microstructure of Ω is considered, yet involving the full reactive system. After a simulated dissolution time of 600 hr, we compare the calculated calcium concentration for a variety of mesh parameters to a reference solution (belonging to the finest meshes). Therefore, the overall mass defect (L^1 error) is determined using quadrature and depicted in Figure 9. Note that all simulations feature the same time stepping scheme. In case of large values of H, a refinement of the microscopic mesh did not lead to an improved approximation quality, indicating misspent computational effort. Conversely, refinement of h does significantly reduce the error for small values of H, again indicating badly balanced computation time. In Table 1, the convergence behavior with respect to

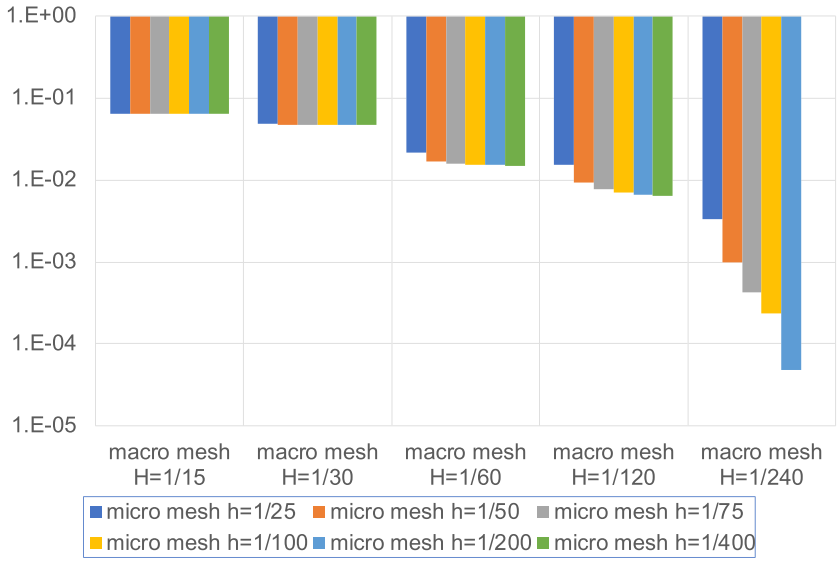

Figure 9. Comparison of quality of solutions calculated with different mesh parameters h, H, showing relative L^1 error in macroscopic calcium concentration to reference solution. Each color refers to a fixed microscopic mesh size.

microscopic and macroscopic mesh parameter is presented quantitatively. There, we additionally consider the corresponding L^2 errors and the estimated order of convergence (EOC) according to the formula

$$\mathrm{EOC}(L^p) = \log_2\left(\frac{||c_j - c_{j+1}||_{L^p}}{||c_{j+1} - c_{j+2}||_{L^p}}\right),$$

where c_j denotes the concentration belonging to the jth refinement level. As expected for lowest-order Raviart-Thomas elements, linear convergence is obtained in H. In the microscopic discretization parameter h a quadratic convergence can be concluded. Such a behavior has already been observed in Ray, Oberlander, et al. (2019) but only as superconvergence in an isotropic dissolution scenario. We therefore conclude quadratic convergence to be the result of the second-order level-set solver. In the realm of multiscale finite elements, convergence results with optimal order in both microscopic and macroscopic discretization parameters are known and also proven for elliptic equations (Hesthaven et al., 2014). Therefore, quadratic

Table 1
Errors and EOC in Calcium Concentration w.r.t. to the Microscopic and Macroscopic Discretization Parameters h, H at Pe = 5,000

Convergence in H at $h = 1/400$						
H	$\|c_{\mathrm{Ca}_{i-1}} - c_{\mathrm{Ca}_i}\|_{L^2}$	$\frac{\|c_{\mathrm{Ca}_{i-1}} - c_{\mathrm{Ca}_i}\|_{L^2}}{\|c_{\mathrm{Ca}_i}\|_{L^2}}$	EOC (L^2)	$\|c_{\mathrm{Ca}_{i-1}} - c_{\mathrm{Ca}_i}\|_{L^1}$	$\frac{\|c_{\mathrm{Ca}_{i-1}} - c_{\mathrm{Ca}_i}\|_{L^1}}{\|c_{\mathrm{Ca}_i}\|_{L^1}}$	EOC (L^1)
$\frac{1}{15}$	—	—	—	—	—	—
$\frac{1}{30}$	3.9581e−8	1.2957e−1	—	1.4166e-9	7.7043e−2	—
$\frac{1}{60}$	2.7826e−8	9.0779e−2	0.5133	8.9232e−10	4.8145e−2	0.6783
$\frac{1}{120}$	1.157e−8	3.7757e−2	1.2656	2.8277e−10	1.5275e−2	1.6562
$\frac{1}{240}$	4.8345e−9	1.5765e−2	1.2600	1.1941e−10	6.4462e−3	1.2447
Convergence in h at $H = 1/240$						
h	$\|c_{\mathrm{Ca}_{i-1}} - c_{\mathrm{Ca}_i}\|_{L^2}$	$\frac{\|c_{\mathrm{Ca}_{i-1}} - c_{\mathrm{Ca}_i}\|_{L^2}}{\|c_{\mathrm{Ca}_i}\|_{L^2}}$	EOC (L^2)	$\|c_{\mathrm{Ca}_{i-1}} - c_{\mathrm{Ca}_i}\|_{L^1}$	$\frac{\|c_{\mathrm{Ca}_{i-1}} - c_{\mathrm{Ca}_i}\|_{L^1}}{\|c_{\mathrm{Ca}_i}\|_{L^1}}$	EOC (L^1)
$\frac{1}{25}$	—	—	—	—	—	—
$\frac{1}{50}$	7.0742e−10	2.3091e−3	—	4.2664e−11	2.3053e−3	—
$\frac{1}{100}$	2.2721e−10	7.4110e−4	1.6385	1.3699e−11	7.3970e−4	1.6389
$\frac{1}{200}$	5.7793e−11	1.8847e−4	1.9751	3.4846e−12	1.8811e−4	1.9751
$\frac{1}{400}$	1.4660e−11	4.7807e−5	1.9790	8.8395e−13	4.7718e−5	1.9789

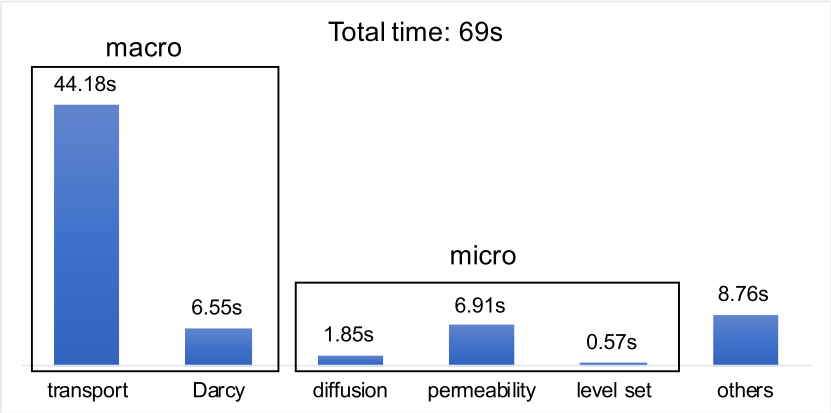

Figure 10. Computation time spent on solving different subproblems for mesh parameters $h = 1/50$, $H = 1/70$. In this test scenario, one complete reevaluation of the single microcell is enforced. Entity of micro subproblems requires a subordinate amount of computation time.

convergence estimates in h are expected in our application, although the diffusion solver used is only linearly convergent. Since the examples provided deal with highly advection dominated transport (Pe = 5,000), those linear contributions seem to play a subordinate role up to the resolutions considered. However, the macroscopic solution is more sensitive to H than h. Taking sensitivity and order of convergence into account, a meaningful relation between the microscopic and macroscopic mesh parameters can be deduced as done in Hesthaven et al. (2014). Using the data presented in Figure 9, we deduce the recommendation $h^2 \sim \frac{H}{30}$ as a rule of thumb for our further calculations in order to keep the errors related to the microscopic mesh considerably lower than those arising from the macroscopic discretization. Certainly, this proportionality factor depends in general on the input parameters.

In order to underline the efficiency of our solution algorithm, we analyze the time spent on each subproblem in case of a reasonable h,H relation; see Figure 10. For this simulation all adaptivity features are disabled, enforcing the solution of the single cell problem at each time step. In fact, the amount of computational time invested in gaining supporting information from the microscale accounts for about 15% of the total time. Exploitation of weak scalability and application of adaptive methods (see section 3.4.2) will approximately preserve this ratio as the number of cell problems increases. In Table 2, computation times for a constant number of cells-CPU cores ratio are depicted as achieved by exploitation of parallel for-loops in MATLAB©. Up to 16 cores a reasonable parallel efficiency is achieved. In the realm of higher parallelization on our test system, the effects of internodal transport and load imbalance seem to play an important role but might be mitigated by refined parallelization methods. An overview of commonly encountered performance bottlenecks in parallel computing is given in Rajput and Katiyar (2013).

Table 2
Weak Scalability in the Number of Cell Problems

Number of cores	Time in s	Parallel efficiency
1	85.5	1
2	90.5	0.945
4	91.9	0.930
8	93.4	0.915
16	101.1	0.846
32	149.7	0.571

Note. Total time spent on microcalculations for different numbers of CPU cores in seconds. Computation of twice as many cell problems as cores with micromesh parameter $h = 1/64$. Calculations performed on a four NUMA-node system, each node powered by an Intel® Xeon® E7-4870 CPU.

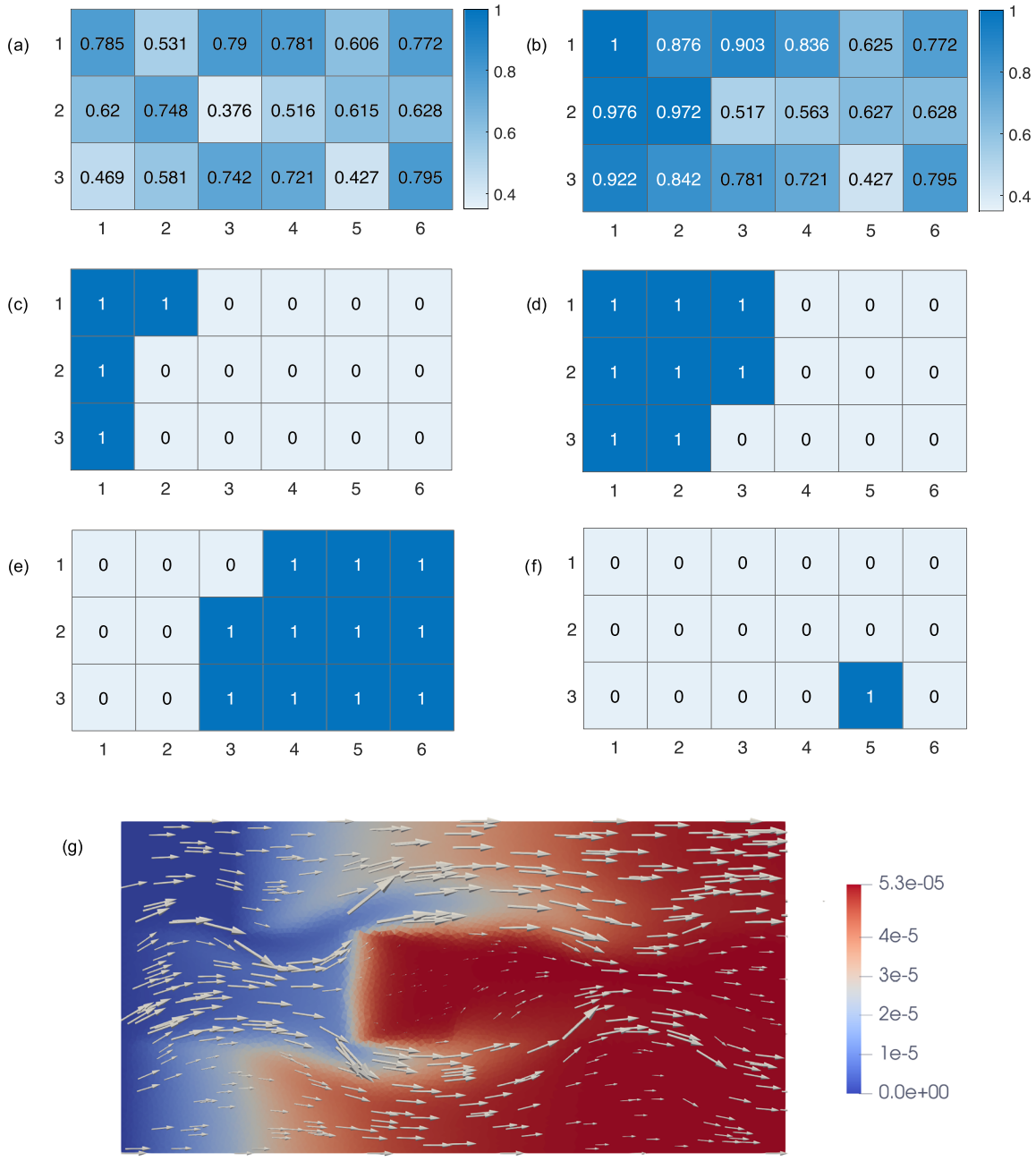

Figure 11. Dissolution of a random porosity field: The top row illustrates a porosity map of the macroscopic domain Ω at time steps 0 (a) and 25 (b). Images (c–f) depict the recalculated cell problems in dark blue for the following time steps: 17 (c), 20 (d), 30 (e), and 40 (f). The label "1" corresponds to a complete reevaluation of permeability and diffusion tensors for the related micro cell. In (g) the calcium concentration in mol dm^{-2} at time step 25 (blue/low to red/high concentration) is shown. Nonparallel stream lines (gray arrows) are visible due to a nonuniform permeability field.

Considering the effects of adaptivity and weak scalability, our micro-macro simulation is comparable to pure macroscale models in terms of computation time.

5.2. Random Porosity Field and Adaptivity Testing

In the following, we consider the macroscopic domain Ω being subdivided into an array of 6×3 squares. A microcell is attached to each of them and initialized with a quadratic solid of random size, such that the arising porosities are randomly distributed in the interval [0.36,0.80] (Figure 11a). In this example, we examine the development of the local porosities as the dolomite structure deteriorates under the inflow of an acidic liquid over the left boundary. A coarse time discretization is chosen in this purely illustratory example

in order to clearly demonstrate the functionality of the adaptivity procedure. As expected, the porosity rises fastest in proximity of the inlet. Far away from the left boundary, the concentration of solutes is already close to equilibrium inhibiting the dissolution process; see Figure 11b.

In this scenario, 70% of computational effort related to cell evaluations was saved by the methods of adaptivity presented in section 3.4.2. As in Ray, Oberlander, et al. (2019), the initial data of the transport equations are far away from equilibrium. Therefore, an exponential time stepping capped at a maximal step size was used. Since the time scale of dissolution reactions is orders of magnitude larger than the initial time step, no reevaluation of the cell problems (8) and (9) was necessary within the first 16 steps. In the course of the simulation, the dissolution front migrates toward the right boundary. Our efficient solution algorithm concentrates computational effort on the cell problems related to this moving front. In Figures 11c–11f, regions with recalculated cell problems are highlighted for different time steps. In total, 515 out of 720 solver calls were saved.

As already mentioned in section 4.2, nonuniform permeability conditions in Ω will lead to distortions in the flow field, influencing solutes' transport. In Figure 11g, the concentration of calcium ions within the liquid is depicted. Comparing to the porosity maps in Figures 11a and 11b, regions of lower permeability show a stronger accumulation of calcium. Moreover, curved flow lines are visible, focusing transport to areas of high permeability, which could not be accounted for in Ray, Oberlander, et al. (2019). Since the solutes' concentration distribution determines local dissolution speeds, major improvements on accuracy are expected by solving Darcy's equation.

5.3. Comparison to Pore-Scale Simulation

In this section, we compare our micro-macro algorithm with a purely microscopic simulation in terms of computational effort and accuracy. In order to solve the microscopic equations presented in (3), we extended the HyPHM solvers to work on domains implicitly given by a level-set function. This allows for a direct coupling to the level-set solver. Exploiting the local conservation properties of our discretization for the transport equation, an equivalent rewriting of the interior boundary conditions as local source terms allows for the usage of the aforementioned Newton solver without further adaptations. This reformulation is commonly used in finite volume methods; see Moukalled et al. (2016). For the evaluation of the Stokes problem, we exploit the same algorithm used within the permeability solver. In this case, a first-order level-set solver is applied to account for the lower smoothness of the velocity field. Nevertheless, roughness has been counteracted by projecting the concentration field into the solid before calculating the normal velocity globally on Ω according to the formula presented in (2) (cf. Li et al., 2008). The quality of this algorithm has been assessed by comparison to the benchmarks presented in Molins et al. (2020). Predicted dissolution rates in a static scenario (Benchmark Part I) as well as solid deformation in a dynamic case (Benchmark Part II) are in good agreement with our calculations.

In the following, we consider the dissolution process of an array of dolomite grains, similar to test scenarios found in the literature (Molins et al., 2017; Ray, Oberlander, et al., 2019). In particular, 27×13 circular grains are arranged within the rectangular domain Ω representing a dolomite structure with a porosity of 0.75; see Figure 12a. In order to illustrate the applicability of our micro-macro simulation to realistic scenarios like flow-channel experiments, we refrained from choosing a perfectly periodic array in terms of a tessellation with reference cells. Instead, columns of grains are shifted against each other; the fringe of the array does not match grain spacing and boundary conditions are nonperiodic. For the microscale simulation, Stokes equations exterior boundary conditions are chosen as follows:

$$\begin{aligned} \vec{v} &= 0 && \text{on } (0,T)\times\Gamma_{\pm}, \\ \vec{v} &= [10^{-2},\ 0]^T \quad [\text{cm/s}] && \text{on } (0,T)\times\Gamma_{\text{in}}, \\ p &= 0 && \text{on } (0,T)\times\Gamma_{\text{out}}, \end{aligned}$$

resulting in a Péclet number of 500. The calculations were performed on a regular 800×400 grid, allowing to capture the shape of each grain properly.

For our micro-macro simulation, slight simplifications are applied exploiting the symmetry of the problem. In anticipation of an effectively one-dimensional dissolution process along the x axis, we assign one unit cell to each column of the array; see Ray, Oberlander, et al. (2019). As depicted in Figure 3b, the macroscopic discretization elements are grouped by the x coordinate of their barycenter and propagate their averaged concentration values to the respective unit cell. Accordingly, the quantities calculated therein are propagated

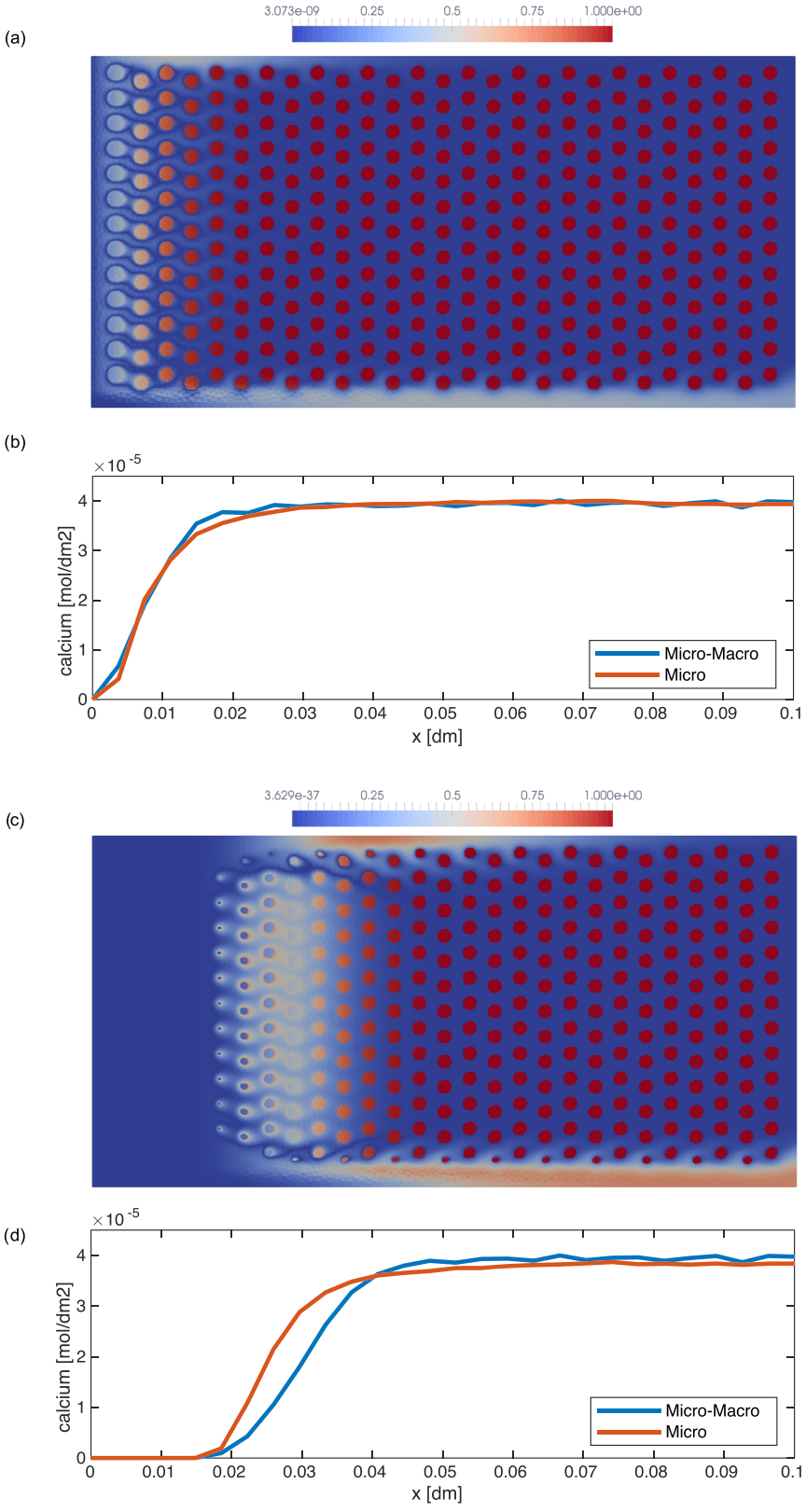

Figure 12. (a) Normalized difference of calcium concentration distribution between micro-macro and pore-scale simulation in Ω after 7 min. For convenience, the microscopic solutes' concentrations in the solid part are extended to zero. The corresponding concentration distributions averaged along the vertical axis are depicted in (b), adjusted for porosity. The same quantities are displayed in (c) and (d) at the final time of 600 hr.

Table 3
Parameters Used in the Micro-Macro Simulation

Parameter	Value
macroscopic domain Ω	$[0,1]\times[0,0.5]\,;[\mathrm{cm}^2]$
number of unit cells	27
cell resolution	64 x 64
microscopic mesh parameter h	1/64
macroscopic resolution	108×54
macroscopic mesh parameter H	1/108 [cm]
inlet velocity	10^{-4} m/s
Péclet number	500
simulation time	$2.16\cdot 10^6$ s
number of time steps	53
initial porosity	0.75
initial unit cell geometry	circular

back to all related macroscopic elements. All solids Y_s are initialized as circles matching the overall porosity of 0.75. Further parameters are listed in Table 3.

We conduct a comparison of both simulation results arising from different modeling approaches similarly to the procedure presented in Molins et al. (2020). First, we look at the static scenario, that is, short simulation times without substantial changes to the underlying microstructure. In Figures 12a and 12b, the predicted calcium concentration field by micro-macro and pore-scale simulations are compared after a time of 7 min, referring to the fourth time step. Since the inflow velocity is quite low in comparison to the reaction speed, we expect mineral and liquid to reach chemical equilibrium quickly as the solutes are transported toward the right boundary. It is evident from illustration (b) in Figure 12 that our micro-macro simulation captures the position and slope of the dissolution front quite accurately. Minor deviations at the fringe of the dissolution front might be caused by boundary effects in the bottom part of the domain where the distance between the array and the boundary is particularly large or due to insufficient spatial resolution of the macrodomain in this area. Note that the dissolution front in case of our micro-macro simulation is only resolved by about 20 finite elements in diameter. Since the predicted concentrations are almost equal in proximity to the outflow boundary, similar speeds of the dissolution fronts are expected due to mass conservation. From these data a total dissolution time of the array of approximately $8\cdot 10^6$ s is deduced.

In a second step, we investigate the long-term behavior of both solutions. For that reason, a time horizon of 600 hr is chosen, expecting the dissolution front to move approximately 2.5 mm toward the right boundary. For both simulations an identical time stepping scheme is applied. After an exponential growing phase to basis two starting from an initial time step of 60 s, step sizes are capped at 50,000 s. As it is deduced from the results of the static experiment, this temporal discretization should allow for each dolomite grain to dissolve within several time steps. Therefore, the operator splitting error between transport and domain evolution is reasonably small. As the implicit Euler method is unconditionally stable, there are no theoretical restrictions on the time step size. Again, normalized deviation between both solutions as well as a comparison of the horizontal concentration distribution are depicted in Figures 12c and 12d. According to our prediction, both dissolution fronts move to the right, still commencing at the same value of x. As it is evident from image Figure 12c, boundary effects in the microscale simulation distorted the front. Instead of a vertical course, roundings have formed close to the lateral flow boundary. Moreover, deviations in the width of the dissolution front as well as the total outflow of mass are detected. Nevertheless, both simulations are in good agreement considering the massive difference in computational effort invested.

To close the comparison of both simulation and modeling methods, we dedicate ourselves to the computation times. Aforementioned micro-macro simulation was executed on a system running an `Intel® Core™` i7-4790 CPU with a base clock of 3.6 GHz and 16 GB of ram. A total run time of 780 s was measured. In contrast, the microscale computations were performed on an `Intel® Xeon®` E5-2630 v4 at 2.2 GHz base clock and 126 GB of ram due to the enormous memory consumption of the Newton solver. Here, a total run time of 27,300 s was identified. In both cases, most of the computation time was spent on the nonlinear transport problem. For the sake of a reasonable comparison in computation time, the micro-macro simulation was performed on the server CPU as well, terminating after 1,080 s. Hence, the micro-macro simulation presented in this paper has shown to be about 25 times faster.

6. Conclusion

In this paper, we proposed an efficient numerical scheme for reactive flow and transport problems in evolving heterogeneous porous media. Based on a detailed microscopic model and its upscaling, an algorithm has been developed accounting for the bidirectional coupling of the inherent microscale and macroscale. Building upon recent research, existing approaches are extended by taking nonhomogeneous permeability conditions and therefore nontrivial flow fields into account. Since it is evident that there cannot be a simple Kozeny-Carman type relation delivering good approximations for a variety of geometries

(Schulz et al., 2019), detailed microscopic information is needed and must be taken into account to achieve high accuracy. Our algorithm is well suited to properly account for complex solid geometries of the underlying microstructure. In this way, situations going beyond the applicability of classical substitutional power laws for macroscopic parameters such as Kozeny-Carman are accessible. Throughout our elaborations a special emphasis has been laid on efficiency. Thanks to a parallel treatment of the cell problems and a tailored adaptivity scheme, we could prove computational time of our micro-macro approach to be comparable to purely macroscopic simulations. Furthermore, a comparison to pure microscale simulations in a realistic test scenario has been performed, underlining the predictive power of our simulation in terms of accuracy. Current research addresses dissolution and precipitation reactions involving several minerals. The direct interaction of different solid phases naturally leads to unsymmetrical and irregular geometries, which can be tackled numerically with the methods described in this paper. Future research will entail error analysis for the presented numerical scheme.

Data Availability Statement

The data associated with this paper will be made available via 4TU.Center for Research Data.

Acknowledgments
This research was supported by the DFG Research Training Group 2339 Interfaces, Complex Structures, and Singular Limits. We further acknowledge the helpful discussions with Florian Frank, who also provided his toolbox HyPHM. We also thank the anonymous reviewers for their detailed comments helping to clarify and complement our presentation. The second author was supported by VEGA 1/0709/19. Open access funding enabled and organized by Projekt DEAL.

References

Ahkami, M., Roesgen, T., Saar, M., & Kong, X.-Z. (2018). High-resolution temporo-ensemble PIV to resolve pore-scale flow in 3D-printed fractured porous media. *Transport in Porous Media*, *129*, 467–483.

Bastidas, M., Bringedal, C., & Pop, I. S. (2020). Numerical simulation of a phase-field model for reactive transport in porous media: UHasselt Computational Mathematics Preprint. https://www.uhasselt.be/Documents/CMAT/Preprints/2020/UP2002.pdf

Bastidas, M., Bringedal, C., Pop, I., & Radu, F. (2019). Adaptive numerical homogenization of non-linear diffusion problems: UHasselt Computational Mathematics Preprint. https://www.uhasselt.be/Documents/CMAT/Preprints/2019/UP1904.pdf

Battiato, I., Tartakovsky, D. M., Tartakovsky, A. M., & Scheibe, T. (2009). On breakdown of macroscopic models of mixing-controlled heterogeneous reactions in porous media. *Advances in Water Resources*, *32*(11), 1664–1673.

Battiato, I., Tartakovsky, D. M., Tartakovsky, A. M., & Scheibe, T. D. (2011). Hybrid models of reactive transport in porous and fractured media. *Advances in Water Resources*, *34*(9), 1140–1150.

Bollhöfer, M., & Saad, Y. (2006). Multilevel preconditioners constructed from inverse-based ILUs. *SIAM Journal on Scientific Computing*, *27*, 1627–1650.

Bringedal, C., Berre, I., Pop, I. S., & Radu, F. A. (2016). Upscaling of non-isothermal reactive porous media flow with changing porosity. *Transport in Porous Media*, *114*(2), 371–393.

Bringedal, C., & Kumar, K. (2017). Effective behavior near clogging in upscaled equations for non-isothermal reactive porous media flow. *Transport in Porous Media*, *120*(3), 553–577. https://doi.org/10.1007/s11242-017-0940-y

Bringedal, C., von Wolff, L., & Pop, I. (2019). Phase field modeling of precipitation and dissolution processes in porous media: Upscaling and numerical experiments: UHasselt Computational Mathematics Preprint. https://www.uhasselt.be/Documents/CMAT/Preprints/2019/UP1901.pdf

Duintjer Tebbens, J., & Tůma, M. (2007). Efficient preconditioning of sequences of nonsymmetric linear systems. *SIAM Journal on Scientific Computing*, *29*, 1918–1941.

Weinan, E., Engquist, B., Li, X., Ren, W., & Vanden-Eijnden, E. (2007). Heterogeneous multiscale methods: A review. *Communications in Computational Physics*, *2*, 367–450.

Ebigbo, A., Helmig, R., Cunningham, A. B., Class, H., & Gerlach, R. (2010). Modelling biofilm growth in the presence of carbon dioxide and water flow in the subsurface. *Advances in Water Resources*, *33*(7), 762–781.

Ellis, B., Peters, C., Fitts, J., Bromhal, G., McIntyre, D., Warzinski, R., & Rosenbaum, E. (2011). Deterioration of a fractured carbonate caprock exposed to CO_2-acidified brine flow. *Greenhouse Gases: Science and Technology*, *1*(3), 248–260.

Frank, F. (2013). Numerical studies of models for electrokinetic flow and charged solute transport in periodic porous media (Ph.D. Thesis), Friedrich-Alexander-Universität Erlangen-Nürnberg (FAU). https://d-nb.info/1054331324/34

Frank, F. (2014). HyPHM. Chair of Applied Mathematics 1, University of Erlangen–Nuremberg. http://www1.am.uni-erlangen.de/HyPHM, (Accessed: June 18, 2020).

Frolkovič, P. (2012). Application of level set method for groundwater flow with moving boundary. *Advances in Water Resources*, *47*, 56–66.

Gärttner, S., Frolkovič, P., Knabner, P., & Ray, N. (2020). Efficiency and accuracy of micro-macro models for mineral dissolution/precipitation: Preprint-Reihe Angewandte Mathematik University Erlangen-Nürnberg. https://www1.am.uni-erlangen.de/research/preprint/pr407.pdf

Golfier, F., Zarcone, C., Bazin, B., Lenormand, R., Lasseux, D., & Quintard, M. (2002). On the ability of a Darcy-scale model to capture wormhole formation during the dissolution of a porous medium. *Journal of Fluid Mechanics*, *457*, 213–254. https://doi.org/10.1017/S0022112002007735

Guibert, R., Horgue, P., Debenest, G., & Quintard, M. (2016). A comparison of various methods for the numerical evaluation of porous media permeability tensors from pore-scale geometry. *Mathematical Geosciences*, *48*(3), 329–347.

Hesthaven, J., Zhang, S., & Zhu, X. (2014). High-order multiscale finite element method for elliptic problems. *SIAM Journal on Multiscale Modeling and Simulation*, *12*, 650–666.

Hornung, U. (Ed.) (1997). *Homogenization and porous media*. New York, Berlin, Heidelberg: Springer-Verlag.

Japhet, C., Cuvelier, F., & Scarella, G. (2013). An efficient way to perform the assembly of finite element matrices in Matlab and Octave. HAL. https://hal.archives-ouvertes.fr/hal-00785101v1/document

Kim, H., & Swan, C. (2003). Voxel-based meshing and unit-cell analysis of textile composites. *International Journal for Numerical Methods in Engineering*, *56*, 977–1006. https://doi.org/10.1002/nme.594

Koko, J. (2019). Efficient MATLAB codes for the 2D/3D Stokes equation with the mini-element. *Informatica, Lithuanian Academy of Sciences*, *30*, 243–268.

Kumar, K., van Noorden, T. L., & Pop, I. S. (2011). Effective dispersion equations for reactive flows involving free boundaries at the microscale. *Multiscale Modeling & Simulation*, *9*(1), 29–58. https://doi.org/10.1137/100804553

Li, X., Huang, H., & Meakin, P. (2008). Level set simulation of coupled advection-diffusion and pore structure evolution due to mineral precipitation in porous media. *Water Resources Research*, *44*, W12407. https://doi.org/10.1029/2007WR006742

Li, X., Huang, H., & Meakin, P. (2010). A three-dimensional level set simulation of coupled reactive transport and precipitation/dissolution. *International Journal of Heat and Mass Transfer*, *53*(13-14), 2908–2923.

Li, Z., & Song, P. (2012). An adaptive mesh refinement strategy for immersed boundary/interface methods. *Communications in computational physics*, *12*, 515–527. https://doi.org/10.4208/cicp.070211.150811s

MATLAB (2019). *Version 9.6.0.1072779 (R2019a)*. Natick, Massachusetts: The MathWorks Inc.

Michaowski, T., & Garcia Asuero, A. (2012). Thermodynamic modelling of dolomite behavior in aqueous media. *Journal of Thermodynamics*, *2012*, 723,052.

Molins, S., & Knabner, P. (2019). Multiscale approaches in reactive transport modeling. *Reviews in Mineralogy & Geochemistry*, *85*, 27–48.

Molins, S., Soulaine, C., Prasianakis, N., Abbasi, A., Poncet, P., Ladd, A., et al. (2020). Simulation of mineral dissolution at the pore scale with evolving fluid-solid interfaces: Review of approaches and benchmark problem set. *Computational Geosciences*. https://doi.org/10.1007/s10596-019-09903-x

Molins, S., Trebotich, D., Miller, G. H., & Steefel, C. I. (2017). Mineralogical and transport controls on the evolution of porous media texture using direct numerical simulation. *Water Resources Research*, *53*, 3645–3661. https://doi.org/10.1002/2016WR020323

Moukalled, F., Mangani, L., & Darwish, M. (2016). Implementation of boundary conditions in the finite-volume pressure-based method part i: Segregated solvers. *Numerical Heat Transfer, Part B: Fundamentals*, *69*(6), 534–562.

Muntean, A., & van Noorden, T. L. (2013). Corrector estimates for the homogenization of a locally periodic medium with areas of low and high diffusivity. *European Journal of Applied Mathematics*, *24*(5), 657–677.

Osher, S., & Fedkiw, R. (2006). *Level set methods and dynamic implicit surfaces* (Vol. 153). New York: Springer Science & Business Media.

Osher, S., & Sethian, J. A. (1988). Fronts propagating with curvature-dependent speed: Algorithms based on Hamilton-Jacobi formulations. *Journal of Computational Physics*, *79*, 12–49.

Rajput, V., & Katiyar, A. (2013). Proactive bottleneck performance analysis in parallel computing using openMP. *International Journal of Advanced Studies in Computer Science and Engineering*, *2*, 2013.

Ray, N., Oberlander, J., & Frolkovic, P. (2019). Numerical investigation of a fully coupled micro-macro model for mineral dissolution and precipitation. *Computational Geosciences*, *23*, 1173–1192.

Ray, N., Rupp, A., Schulz, R., & Knabner, P. (2018). Old and new approaches predicting the diffusion in porous media. *Transport in Porous Media*, *124*(3), 803–824. https://doi.org/10.1007/s11242-018-1099-x

Ray, N., & Schulz, R. (2019). Derivation of an effective dispersion model for electroosmotic flow involving free boundaries in a thin strip. *Journal of Engineering Mathematics*, *119*, 167–197.

Ray, N., van Noorden, T., Frank, F., & Knabner, P. (2012). Multiscale modeling of colloid and fluid dynamics in porous media including an evolving microstructure. *Transport in Porous Media*, *95*(3), 669–696.

Ray, N., van Noorden, T., Radu, F. A., Friess, W., & Knabner, P. (2013). Drug release from collagen matrices including an evolving microstructure. *ZAMM-Journal of Applied Mathematics and Mechanics/Zeitschrift für Angewandte Mathematik und Mechanik*, *93*(10-11), 811–822.

Redeker, M. (2014). Adaptive two-scale models for processes with evolution of microstructures (Ph.D. Thesis), Universität Stuttgart. https://elib.uni-stuttgart.de/bitstream/11682/5145/1/dissertation.pdf

Redeker, M., & Eck, C. (2013). A fast and accurate adaptive solution strategy for two-scale models with continuous inter-scale dependencies. *Journal of Computational Physics*, *240*, 268–283.

Rouy, E., & Tourin, A. (1992). A viscosity solutions approach to shape-from-shading. *SIAM Journal on Numerical Analysis*, *29*(3), 867–884.

Rumble, J. R. (2018). *Crc handbook of chemistry and physics*. Boca Raton, Florida: CRC Press.

Sauerland, H. (2013). An XFEM based sharp interface approach for two-phase and free-surface flows (Ph.D. Thesis), Rheinisch-Westfälische Technische Hochschule Aachen. https://d-nb.info/1129875881/34

Schulz, R., & Knabner, P. (2017a). Derivation and analysis of an effective model for biofilm growth in evolving porous media. *Mathematical Methods in the Applied Sciences*, *40*(8), 2930–2948.

Schulz, R., & Knabner, P. (2017b). An effective model for biofilm growth made by chemotactical bacteria in evolving porous media. *SIAM Journal on Applied Mathematics*, *77*(5), 1653–1677.

Schulz, R., Ray, N., Frank, F., Mahato, H. S., & Knabner, P. (2017). Strong solvability up to clogging of an effective diffusion-precipitation model in an evolving porous medium. *European Journal of Applied Mathematics*, *28*(2), 179–207.

Schulz, R., Ray, N., Zech, S., Rupp, A., & Knabner, P. (2019). Beyond Kozeny Carman: Predicting the permeability in porous media. *Transport in Porous Media*, *130*, 487–512.

Sehgal, S., Singh, H., Agarwal, M., Bhasker, V., & Shantanu (2014). Data analysis using principal component analysis. In *2014 international conference on medical imaging, m-health and emerging communication systems (medcom)* (pp. 45–48).

Seigneur, N., Mayer, K. U., & Steefel, C. I. (2019). Reactive transport in evolving porous media. *Reviews in Mineralogy and Geochemistry*, *85*, 197–238.

Sethian, J. A. (1998a). Fast marching methods. *SIAM Review*, *41*, 199–235.

Sethian, J. A. (1998b). Fast marching methods and level set methods for propagating interfaces. von Karman Institute Lecture Series, Computational Fluid Mechanics.

Sethian, J. A. (1999). *Level set methods and fast marching methods: Evolving interfaces in computational geometry, fluid mechanics, computer vision, and materials science* (Vol. 2). Cambridge: Cambridge University Press.

Sobera, M. P., & Kleijn, C. R. (2006). Hydraulic permeability of ordered and disordered single-layer arrays of cylinders. *Physical Review E*, *74*, 036,301.

Soulaine, C., Roman, S., Kovscek, A., & Tchelepi, H. A. (2017). Mineral dissolution and wormholing from a pore-scale perspective. *Journal of Fluid Mechanics*, *827*, 457–483. https://doi.org/10.1017/jfm.2017.499

Soulaine, C., Roman, S., Kovscek, A., & Tchelepi, H. A. (2018). Pore-scale modelling of multiphase reactive flow: Application to mineral dissolution with production of CO_2. *Journal of Fluid Mechanics*, *855*, 616–645. https://doi.org/10.1017/jfm.2018.655

Steefel, C. I., Beckingham, L. E., & Landrot, G. (2015). Micro-continuum approaches for modeling pore-scale geochemical processes. *Reviews in Mineralogy and Geochemistry*, *80*(1), 217–246.

Tartakovsky, A. M., Tartakovsky, D. M., Scheibe, T. D., & Meakin, P. (2008). Hybrid simulations of reaction-diffusion systems in porous media. *SIAM Journal on Scientific Computing*, *30*(6), 2799–2816.

van Noorden, T. L. (2009a). Crystal precipitation and dissolution in a porous medium: Effective equations and numerical experiments. *Multiscale Modeling & Simulation*, *7*(3), 1220–1236.

van Noorden, T. L. (2009b). Crystal precipitation and dissolution in a thin strip. *European Journal of Applied Mathematics*, *20*(1), 69–91.

van Noorden, T. L., Pop, I. S., Ebigbo, A., & Helmig, R. (2010). An upscaled model for biofilm growth in a thin strip. *Water Resources Research*, *46*, W06505. https://doi.org/10.1029/2009WR008217

WWW-MINCRYST (2014). Institute of experimental mineralogy, www-mincryst, crystallographic and crystallochemical database for minerals and their structure analogues. http://database.iem.ac.ru/mincryst/s_carta.php?DOLOMITE+1257 (accessed: December 4th, 2019)

Wang, J. H. (1965). Self-diffusion coefficients of water. *The Journal of Physical Chemistry*, *69*(12), 4412–4412.

Xiong, Q., Baychev, T. G., & Jivkov, A. P. (2016). Review of pore network modelling of porous media: experimental characterisations, network constructions and applications to reactive transport. *Journal of Contaminant Hydrology*, *192*, 101–117.

Xu, Z., Huang, H., Li, X., & Meakin, P. (2012). Phase field and level set methods for modeling solute precipitation and/or dissolution. *Computer Physics Communications*, *183*(1), 15–19.